

# Perovskite-type superlattices from lead-halide perovskite nanocubes

Ihor Cherniukh<sup>1,2</sup>, Gabriele Rainò<sup>1,2</sup>, Thilo Stöferle<sup>3</sup>, Max Burian<sup>4</sup>, Alex Travasset<sup>5</sup>, Denys Naumenko<sup>6</sup>, Heinz Amenitsch<sup>6</sup>, Rolf Erni<sup>7</sup>, Rainer F. Mahrt<sup>3</sup>, Maryna I. Bodnarchuk<sup>1,2</sup>, Maksym V. Kovalenko<sup>1,2\*</sup>

<sup>1</sup>Department of Chemistry and Applied Bioscience, Institute of Inorganic Chemistry, ETH Zürich, Zürich, Switzerland.

<sup>2</sup>Laboratory of Thin Films and Photovoltaics, Empa – Swiss Federal Laboratories for Materials Science and Technology, Dübendorf, Switzerland.

<sup>3</sup>IBM Research Europe — Zurich, Rüschlikon, Switzerland.

<sup>4</sup>Swiss Light Source, Paul Scherrer Institut, Villigen PSI, Switzerland.

<sup>5</sup>Department of Physics and Astronomy, Iowa State University and Ames Lab, Ames, Iowa, USA.

<sup>6</sup>Institute of Inorganic Chemistry, Graz University of Technology, Graz, Austria.

<sup>7</sup>Electron Microscopy Center, Empa – Swiss Federal Laboratories for Materials Science and Technology, Dübendorf, Switzerland

This document is the accepted manuscript version of the following article:

Cherniukh, I., Rainò, G., Stöferle, T., Burian, M., Travasset, A., Naumenko, D., ... Kovalenko, M. V. (2021). Perovskite-type superlattices from lead halide perovskite nanocubes. *Nature*, 593(7860), 535–542. <https://doi.org/10.1038/s41586-021-03492-5>

For over 80 years, tailored molecular assemblies (*e.g.*, H- and J-aggregates) have been of interest for the emergence of collective phenomena in their optical spectra<sup>1</sup>, coherent long-range energy transport<sup>2,3</sup> and their conceptual similarity with natural light-harvesting complexes<sup>4,5</sup>. Another highly versatile platform for creating controlled, aggregated states exhibiting collective phenomena arises from the organization of colloidal semiconductor nanocrystals (NCs) into long-range ordered superlattices (SLs)<sup>6</sup>. Cesium lead halide perovskite NCs<sup>7-9</sup> have recently emerged as highly appealing building blocks, owing to their high oscillator strength<sup>10</sup>, slow dephasing (long coherence times of up to 80 ps)<sup>11,12</sup>, minimal inhomogeneous broadening of emission lines, and a bright triplet exciton character with orthogonal dipole orientation<sup>10</sup>, potentially enabling an efficient omnidirectional coupling. Here we present perovskite-type (ABO<sub>3</sub>) binary and ternary NC SLs by a shape-directed co-assembly of steric-stabilized, highly luminescent cuboid-shaped CsPbBr<sub>3</sub> NCs (occupying B- and/or O-sites) with spherical Fe<sub>3</sub>O<sub>4</sub> or NaGdF<sub>4</sub> NCs (A-sites) and truncated-cuboid PbS NCs (B-site). Such ABO<sub>3</sub> SLs, as well as other newly obtained SL structures (binary NaCl- and AlB<sub>2</sub>-types), exhibit a high degree of orientational ordering of CsPbBr<sub>3</sub> nanocubes. These novel perovskite mesostructures exhibit superfluorescence (SF) – a collective emission resulting in a burst of photons. SF is characterized, at high excitation density, by emission pulses with ultrafast (22 ps) radiative decay and Burnham-Chiao ringing behaviour with a strongly accelerated build-up time.

SF, unlike fluorescence, is a collective emission of several, incoherently photo-excited dipoles mediated by their common photon field, and is characterized by faster radiative lifetimes and the appearance of Burnham-Chiao ringing behaviour<sup>13</sup>. Previously, these features could be realized either in the gaseous state (HF gas)<sup>14</sup> or in a limited number of solid-state systems (CuCl-doped NaCl, peroxide-ion-doped KCl, and epitaxial InGaAs quantum wells)<sup>15-17</sup>. SF in lead halide perovskite NC SLs was recently demonstrated with the simplest packing geometry – simple cubic packing (*scp*) of cubic NCs into a 3D-supercrystal<sup>13</sup>. Far broader structural engineerability of SLs, required for programmable tuning of the collective emission and for building a theoretical framework, can be envisioned from the recent advancements in colloidal science<sup>6,18,19</sup>.

The formation of NC SLs is generally governed by the balance between the enthalpic contributions and entropic interactions<sup>6</sup>. Enthalpy prevails when, for instance, specific pair-wise interactions between NCs are designed, such as in the aqueous-based co-assembly of DNA-coated noble metal NCs with DNA linkers<sup>20,21</sup>, which is not an applicable strategy to water-degradable perovskite NCs. However, entropy can become a prevailing factor for steric-stabilized apolar NC colloids; that is, when the strong short-range repulsion of hydrocarbon ligand chains is the principle component of the interparticle potential, causing a hard-sphere-like behaviour of NCs. Such colloids often undergo a transition into the densest possible periodic arrays upon solvent evaporation, hexagonal close packing (*hcp*) or face-centred cubic (*fcc*) for spheres<sup>22</sup> or *scp* for cubes (see Ref.<sup>23</sup> and, for perovskite NCs, also Ref.<sup>13,24-27</sup>), maximizing the free-volume entropy of the system<sup>6</sup>. Furthermore, mixtures of spherical NCs were shown to form at least twenty different binary SL structures, usually those with higher packing density for a given ratio of their effective hard-sphere diameters. Typically, SLs that are isostructural with NaCl, NaZn<sub>13</sub>, AlB<sub>2</sub>, MgZn<sub>2</sub> and CaCu<sub>5</sub> are observed<sup>6,18,19,28,29</sup>. Rather surprisingly, there have been no reports on the formation of multicomponent SLs comprising steric-stabilized cubic NCs. For instance, in the case of a NaCl-type SL, a mixture of larger spheres (A) and smaller cubes (B) will yield greater packing density ( $\eta$ ) than that of two (A + B) spheres at any B/A size ratio ( $\gamma = d_B/d_A < 1$ , Fig. 1k and Supplementary Note 1).

In this work, we not only show that co-assembly of cubic and spherical steric-stabilized NCs is experimentally possible, but also that the cubic shape of perovskite NCs leads to a vastly different outcome of such assembly, as compared to all-spherical systems. Specifically, we present perovskite-type (ABO<sub>3</sub>) binary and ternary NC SLs (Figs. 1, 2, 4, 5, Extended Data Figs. 1, 2, 4-7 and Supplementary Figs. 7-12). In binary SLs, larger spherical Fe<sub>3</sub>O<sub>4</sub> or NaGdF<sub>4</sub> NCs occupy the A-sites and smaller cubic CsPbBr<sub>3</sub> NCs reside on both B- and O-sites, whereas in ternary SLs the B-sites

are occupied by truncated-cuboid PbS NCs. We have also obtained NaCl-type SLs (combining 5.3 nm CsPbBr<sub>3</sub> with 14.7-19.8 nm Fe<sub>3</sub>O<sub>4</sub> NCs, and 8.6 nm CsPbBr<sub>3</sub> with 10.2-25.1 nm Fe<sub>3</sub>O<sub>4</sub> and 18.6 nm NaGdF<sub>4</sub> NCs, see Fig. 3 and Supplementary Figs. 13, 14) and AlB<sub>2</sub>-type SLs (in mixtures of 5.3 nm CsPbBr<sub>3</sub> with 12.5 nm Fe<sub>3</sub>O<sub>4</sub> NCs, and 8.6 nm CsPbBr<sub>3</sub> with 19.8 nm Fe<sub>3</sub>O<sub>4</sub> NCs, Extended Data Fig. 3). Importantly, cubic perovskite NCs exhibit a high degree of orientational order within all observed binary SLs. We then demonstrate that these novel perovskite-based mesostructures exhibit SF.

The non-truncated (sharp) cuboid shape of CsPbX<sub>3</sub> NCs – their decisive property for obtaining ABO<sub>3</sub> SLs – arises from the pseudo-cubic faceting of the underlying orthorhombic perovskite lattice as well as various specifics of surface termination and ligand binding (see Ref.<sup>30</sup> and Supplementary Note 2). In order to prevent a sphere-like behaviour in the NC assembly caused by the softening of the cubic NC shape by long-chain ligands typically used for the NC synthesis<sup>31</sup>, the shortest-chain capping ligand that is still capable of both the efficient colloidal stabilization and retention of high photoluminescence (PL) quantum yield, namely didodecyldimethylammonium bromide (DDAB)<sup>30</sup>, was used. The softness ( $\lambda$ ) of a NC can be defined by the ratio of the doubled capping ligand length to the NC diameter ( $d_{core}$ ), or the edge length for cubic NCs ( $l_{core}$ ) (*i.e.*,  $\lambda = 2L/d_{core}$  and  $\lambda = 2L/l_{core}$ , respectively). Monodisperse CsPbBr<sub>3</sub> NCs of two sizes, 5.3 nm ( $\lambda = 0.63$ ) and 8.6 nm ( $\lambda = 0.39$ ), were synthesized as reported previously<sup>30,32</sup> [see transmission electron microscopy (TEM) images and optical characterization in Supplementary Figs. 5 and 6, respectively]. Trials of colloidal crystallization were conducted by controlled solvent evaporation from the mixture of NCs in toluene on various substrates. The structure of the observed SL was characterized with high-angle annular dark-field scanning TEM (HAADF-STEM) at various tilt angles, electron tomography, elemental mapping with energy-dispersive X-ray spectroscopy (EDX-STEM), grazing-incidence small-angle X-ray scattering (GISAXS), scanning electron microscopy (SEM), as well as electron diffraction (ED, wide-angle) and small-angle ED.

### Binary SLs

ABO<sub>3</sub>-type SLs (isostructural with cubic CaTiO<sub>3</sub> perovskite,  $Pm\bar{3}m$  space group) had thus far not been observed in the colloidal crystallization of steric-stabilized NCs. In this lattice, CsPbBr<sub>3</sub> NCs occupy two different Wyckoff positions: 1b (*i.e.*, B-site, with the  $\langle 100 \rangle$  crystallographic directions of the nanocubes aligned with  $\langle 100 \rangle_{SL}$ ; the subscript "SL" denotes the Miller indices of the SL) and 3c (*i.e.*, O-site, two  $\langle 110 \rangle$  aligned with  $\langle 100 \rangle_{SL}$ ). Firstly, 8.6 nm CsPbBr<sub>3</sub> NCs were combined with oleate-capped Fe<sub>3</sub>O<sub>4</sub> NCs (9.6-25.1 nm, Supplementary Fig. 5). Experiments with 9.6-14 nm Fe<sub>3</sub>O<sub>4</sub> NCs yielded separate phases of single-component SLs or disordered mixtures, except for small NaCl-type



domains. With 14.5-20.7 nm  $\text{Fe}_3\text{O}_4$  NCs, however, large domains of  $\text{ABO}_3$ -type SLs were observed (up to  $\sim 100 \mu\text{m}^2$ ; Fig. 1 and Supplementary Fig. 7).  $\text{ABO}_3$ -type SLs were also obtained by combining 8.6 nm  $\text{CsPbBr}_3$  nanocubes with 15.2-19.5 nm  $\text{NaGdF}_4$  NCs (Fig. 5, Extended Data Fig. 2).

Columns of  $\text{CsPbBr}_3$  nanocubes are readily resolved in HAADF-STEM and TEM images as well as from EDX-STEM maps of  $[001]_{\text{SL}}$ -oriented domains (*e.g.*, Fig. 1 and Extended Data Fig. 1). In particular, Z-contrast makes the heavy-element containing  $\text{CsPbBr}_3$  NCs brighter in HAADF-STEM images. EDX-STEM maps also assist in the visualization of the frame of perovskite NCs, showing occupancy of every SL unit cell facet by the O-site nanocube. HAADF-STEM images taken at different tilting angles and compared with simulated projections readily differentiate the binary  $\text{ABO}_3$  lattice from  $\text{CsCl}$ - and  $\text{Li}_3\text{Bi}$ -types (Fig. 2e, f and Supplementary Figs. 8, 9), but do not unambiguously exclude the  $\text{Cu}_3\text{Au}$ -type packing. Full clarity as to occupancy and orientation of the nanocubes was then obtained with ED patterns and respective dark-field TEM images for specific diffraction spots (Fig. 2a-d). The  $\text{Fe}_3\text{O}_4$  NCs exhibit random orientations, apparent from a broad diffraction ring corresponding to the (311) lattice planes. On the contrary, a high degree of orientational order of the  $\text{CsPbBr}_3$  NCs is readily seen as intense arcs corresponding to diffraction on (100), (110), and (200) planes, which are normal to  $\langle 100 \rangle_{\text{SL}}$  and  $\langle 110 \rangle_{\text{SL}}$ . Additionally, the (111) reflections are split into eight maxima with a splitting angle of  $\sim 19.5^\circ$  (reflections "9" and "10" in Fig. 2b). This angle corresponds to the theoretical value for a pair of  $\text{CsPbBr}_3$  cubes located on two orthogonal facets and oriented such that their faces are in contact with the spheres (blue and yellow cubes in Fig. 2c). The centre cubes (B-sites) are rotated  $45^\circ$  with respect to those on the O-sites and hence exhibit distinct reflections (labelled "2" and "4", Fig. 2b). These site occupancies are also confirmed by the dark-field TEM images (Fig. 2d), constructed from the diffraction spots originating from B- or O- positioned cubes ("2,4" and "1,3,6,8,9,10", respectively) or from both ("5,7"). Electron tomography of a small isolated domain further confirms the  $\text{ABO}_3$  structure and visualizes the orientation of B- and O-site cubes (Supplementary Fig. 10 and Supplementary Video 1). Domains exhibiting  $[102]_{\text{SL}}$ ,  $[111]_{\text{SL}}$  and  $[112]_{\text{SL}}$  orientations were also observed (Supplementary Fig. 11). GISAXS measurements show strong, periodic reflections (Fig. 1c), evidencing a high degree of both in-plane and out-of-plane order. The 2D diffraction pattern corresponds to a simple-cubic symmetry ( $Pm\bar{3}m$ ) with a 24.2 nm unit cell (Supplementary Note 3). The in-plane coherent scattering volume, corresponding to the ordered domain size, is  $> 360 \text{ nm}$  (inset in Supplementary Fig. 4a). No structural phase transitions were observed by TEM and ED upon cooling to liquid nitrogen temperature (Supplementary Fig. 12).

With smaller 5.3 nm CsPbBr<sub>3</sub> NCs, which can be considered as "rounded" cubes in the view of their higher softness parameter  $\lambda$ , no ABO<sub>3</sub>-type lattice was observed; rather, lattices that are commonly known for binary mixtures of hard spheres (NaCl- and AlB<sub>2</sub>-types, Supplementary Fig. 13 and Extended Data Fig. 3b-d, respectively). For 8.6 nm CsPbBr<sub>3</sub> combined with 15.6-19.8 nm Fe<sub>3</sub>O<sub>4</sub> NCs, the three ABO<sub>3</sub>-, AlB<sub>2</sub>- (Extended Data Fig. 3e, f) and NaCl-type (Fig. 3) SLs compete. The proportion of AlB<sub>2</sub>- and NaCl-type SLs increases with decreasing perovskite NC particle fraction in the mixture. When the size of A-site spheres is further increased to 25.1 nm, the NaCl-type SL is favoured (Supplementary Fig. 14).

The stability of the binary SLs follows from the analysis of  $\eta$  as a function of  $\gamma$ . The effective sizes of the NCs used for computing  $\gamma$  are calculated by taking into account both the dimension of the inorganic NC core and the ligand shell thickness<sup>33</sup>.  $\eta$  is then calculated following the hard particle formalism, assuming that the ligand shell is space-filling only along the axis connecting two NCs (Optimal Packing Model, OPM) and, in addition, considering the deformability of the ligand shell, namely the bending of ligands away from the axis of contact between NCs (Orbifold Topological Model, OTM)<sup>34,35</sup>. For low coordination numbers, OTM predicts higher  $\eta$  and smaller lattice parameters, in good agreement with experimental values<sup>29</sup>. All-sphere binary SL structures with OPM packing densities above 0.65, sometimes even exceeding the *fcc/hcp* ( $\eta = 0.74$ ), are commonly observed<sup>6,29</sup>. The corresponding range of  $\gamma$ -values is  $\sim 0.3$ - $0.65$ . Very few reports demonstrate SLs at higher  $\gamma$ -values (mainly CaCu<sub>5</sub>- or MgZn<sub>2</sub>-types at  $\gamma = 0.65$ - $0.86$ )<sup>28,36,37</sup>. Interestingly, the OPM packing densities of NaCl-type SLs with cubes on the B-site are  $> 0.705$  across the entire  $\gamma$ -range, unlike all-sphere NaCl-type SLs that are stable and usually observed only at  $\gamma < 0.5$  (Fig. 1k). Indeed, grains of NaCl-type SLs were observed for CsPbBr<sub>3</sub> NCs co-assembled with Fe<sub>3</sub>O<sub>4</sub> NCs for  $\gamma = 0.27$ - $0.73$  (Fig. 3 and Supplementary Figs. 13, 14). Analysis of ED and small-angle ED again reveals the high degree of orientational order of perovskite NCs in a NaCl-type binary SL; for instance, the CsPbBr<sub>3</sub>  $\langle 100 \rangle$  directions coincide with  $\langle 100 \rangle_{\text{SL}}$ .

Although the formation of an ABO<sub>3</sub>-like SL had not been reported and not expected for hard spheres (Fig. 1k), it readily forms with CsPbBr<sub>3</sub> nanocubes at  $\gamma = 0.399, 0.420, 0.477, 0.486, 0.509$  and  $0.541$ . OPM calculations (Fig. 1k) can only explain the first two examples. At  $\gamma \leq \gamma_{c,1} = 0.414$ , the assembly comprises an *scp* lattice of A spheres; cubes can partially rattle in-between, but cannot freely rotate. At  $\gamma > \gamma_{c,1}$ , the shape of the cubes becomes a stronger factor. The cubes are in contact with the spheres (via their facets) and with each other (via sharp vertices) and, according to OTM, ligand vortices form (Supplementary Fig. 2). The overall effect of the cubic shape and ligand deformability is the locking of the cube orientations for both the B- and O-sites as well as much higher packing densities. The OTM

thus explains the formation of ABO<sub>3</sub>-type SLs in a broader  $\gamma$ -range (see the OTM-branch at  $\gamma > 0.414$  in Fig. 1k). The validity of the OTM results is also evident from the better correspondence of the OTM-predicted lattice parameters with the experimental values (Supplementary Table 2 and Supplementary Note 1).

### **Ternary ABO<sub>3</sub>-type SL**

The obtained binary ABO<sub>3</sub> SLs should not be confused with a perovskite-derived Ni<sub>4</sub>N-type due to the non-equivalent orientation of the B- and O-positioned cubes. Furthermore, the centre cube (B-site) also differs in terms of coordination environment. In the case of large spherical A-site NCs, especially at  $\gamma = \gamma_{c,1}$ , the space available for B- and O-cubes is different because O-cubes are in contact with A-spheres, while B-cubes are still rattlers (have freedom to displace themselves around their equilibrium position). This intuition motivated us to explore the possibility of a targeted occupation of the B-site by a larger NC (compared to the O-site), thus yielding a ternary ABO<sub>3</sub>-type SL. For example, the case of a truncated B-site cube with the degree of truncation  $\tau = 0.835$  at  $\gamma_{O/A} = \gamma_{c,1} = 0.414$  and  $\gamma_{B/A} = 0.586$  corresponds to a simultaneous appearance of A-O, A-B, and B-O contacts and a high OPM-packing density of  $\eta = 0.918$ , greatly exceeding the density of a binary lattice at  $\gamma = 0.414$  ( $\eta = 0.808$ ). Experimentally, this was realized herein by combining 10.7 nm truncated cubic PbS NCs with 8.6 nm cubic CsPbBr<sub>3</sub> and 19.8 nm spherical Fe<sub>3</sub>O<sub>4</sub> NCs ( $\gamma_{O/A} = 0.414$ ,  $\gamma_{B/A} = 0.533$ ; Fig. 4, Extended Data Figs. 4, 5). The appearance of B-site PbS NCs is evident from their higher contrast in TEM and HAADF-STEM images in the [001]<sub>SL</sub>, [111]<sub>SL</sub>, [101]<sub>SL</sub> and [112]<sub>SL</sub> orientations. EDX-STEM maps further confirm the incorporation of PbS NCs onto B-sites. Combined ED and small-angle ED analysis indicates that the orientation of the O-site cubes in the ternary SL is the same as in binary SLs. The degree of B-site substitution, as evidenced by ED, is adjustable by increasing the PbS:CsPbBr<sub>3</sub> NC mixing ratio (Fig. 4 and Extended Data Fig. 6).

Atomic perovskite lattices exhibit remarkable structural and compositional engineerability and a close analogy to the presented NC SL system is that of CaTi<sub>(1-x)</sub>Mn<sub>x</sub>O<sub>3</sub> – a B-site solid solution preserving the perovskite *Pnma* symmetry. Larger A-site cations such as Ba<sup>2+</sup>, however, cause phase segregation even at  $x = 0.01$ , driven by the instability of the perovskite phase BaMnO<sub>3</sub><sup>38,39</sup> as the Goldschmidt tolerance factor exceeds the stability range of 0.8-1<sup>40</sup>. Within this understanding, we set to increase the size of the A-site Fe<sub>3</sub>O<sub>4</sub> NCs to emulate this Ca-to-Ba transition. In cases of larger Fe<sub>3</sub>O<sub>4</sub> NC sizes of 21.5 nm ( $\gamma_{B,O/A} = 0.387$ ,  $\eta = 0.755$ ) and 25.1 nm ( $\gamma_{B,O/A} = 0.337$ ,  $\eta = 0.677$ ) combined with 8.6 nm CsPbBr<sub>3</sub> NCs, the OPM packing densities of binary ABO<sub>3</sub> SLs were found to be reduced; seen as a reduced propensity to form SLs (small domains of  $< 0.25 \mu\text{m}^2$ , *ca.* 1% of SL yield). The addition of 11.7 nm PbS NCs ( $\gamma_{B/A} = 0.537$  and

$\gamma_{B/A} = 0.469$ , respectively) led to ternary  $\text{ABO}_3$ -type SLs in high yield and with complete substitution on the B-site (see Extended Data Figs. 6e, f and 7). Thus far, very few examples of ternary SLs had been serendipitously observed for spherical sterically-stabilized NCs (AlMgB<sub>4</sub>-type<sup>41</sup> and bilayered ABC<sub>2</sub>-type<sup>42</sup>). An overarching challenge is to outcompete crystallization into unary and binary SLs. While the formation of multinary solid-state compounds is governed by chemical bonding, NC self-assembly relies on vastly different interactions, wherein shape-anisotropy plays an increasingly important role for obtaining diverse structures, exemplified by the observed strong formability of  $\text{ABO}_3$ -type SLs as well as ABC-type columnar SLs formed by the mixture of disk- and rod-shaped NCs<sup>43</sup>. Preliminary studies combining disks (oleate-capped  $\text{LaF}_3$ ) and  $\text{CsPbBr}_3$  nanocubes yielded six columnar binary SLs, not observed in the disks-spheres mixtures (Extended Data Fig. 8).

### **Superfluorescence from $\text{ABO}_3$ -type SLs**

In molecular aggregates, the weak and broad spectral features of the individual molecules evolve into intense and narrow lines, which are shifted in energy and exhibit enhanced (or suppressed) radiative rates for J-aggregates (or H-aggregates, respectively)<sup>44,45</sup>. Perovskite NCs emerge as an attractive mesoscale alternative for attaining collective behaviour. In particular, 8.6 nm  $\text{CsPbBr}_3$  NCs, co-assembled with spherical  $\text{NaGdF}_4$  NCs into an  $\text{ABO}_3$ -type SL (on  $\text{Si}_3\text{N}_4$ -membranes), exhibit coherent collective emission at low temperatures, upon pulsed excitation (Fig. 5). The emission spectrum comprises two bands (Fig. 5d), of which a narrower and redshifted (by  $\sim 30$  meV) band arises from coupled NCs. Fluence-dependent experiments (inset of Fig. 5d) evidence a linear dependence of the integrated PL intensity, confirming the absence of competing, power-dependent non-radiative processes (*e.g.*, the Auger process) as well as the absence of a threshold that would be commonly associated with amplified spontaneous emission. Drastic shortening of the exciton radiative lifetime and appearance of intensity oscillations with increasing excitation fluence (Fig. 5e, f) attest to the observed emission as being SF. The long exciton coherence, high transition oscillator strength, and low energetic disorder of individual perovskite NCs<sup>10-12</sup> enable coherent coupling of multiple transition dipole moments via a common radiation field, resulting in a single giant dipole, which leads to short and intense bursts of light<sup>13,46</sup>.

The choice of dielectric (non-absorbing) A-site NCs ( $\text{NaGdF}_4$ ) and a dielectric  $\text{Si}_3\text{N}_4$  substrate was found to be crucial for the appearance of SF, since the presence of absorbing materials alter the exciton dynamics at high fluences, presumably by introducing non-radiative channels which quench the PL (see data with the carbon membrane as a substrate in Extended Data Fig. 9). The radiative lifetime is inversely proportional to the number of coherently coupled

NCs,  $N$ , which increases with excitation fluence. Correspondingly, the peak intensity at zero-delay time increases superlinearly over more than two orders of magnitude (Fig. 5h, middle panel). Radiative lifetimes as short as 22 ps can be obtained from spectrally-integrated time-resolved PL (Fig. 5g, h) based on a phenomenological decay model<sup>13</sup>. Furthermore, a shortening of the SF build-up time, after which the photon burst is emitted, is observed (Fig. 5h). This build-up time indicates the time it takes for individual dipoles to phase-lock by interacting via the common photon field; it scales with  $N$  according to  $\tau_{\text{build-up}} \propto (\ln N)/N$ . A good fit to experimental data can be obtained by using this theoretical expression and assuming  $N$  to be proportional to the excitation fluence. Interestingly, the characteristic SF speed-up and oscillations could be retained up to 105 K (Fig. 5i), albeit with a higher fluence required for their emergence. This is likely the result of exciton-phonon interactions, which accelerate the exciton dephasing time, rendering the collective coupling less efficient. For example, a much slower SF build-up time is found at 105 K (Fig. 5i), which eventually becomes longer than the exciton dephasing time such that SF vanishes entirely at higher temperatures. ABO<sub>3</sub>-type SLs exhibit superior collective emission when compared to NaCl-type SLs (Supplementary Note 4, Extended Data Fig. 10), which we attribute to higher perovskite NC-to-dielectric NC ratio (4:1 vs. 1:1) and much reduced perovskite NC-to-NC distance (higher perovskite NC density), which facilitate the occurrence of coherent coupling. In addition, SF from ABO<sub>3</sub>-type SLs can be qualitatively altered, namely shifted from lower to higher energies compared to excitonic PL, simply by increasing the size of NaGdF<sub>4</sub> NCs (Supplementary Note 4; Extended Data Fig. 10). We expect that further atomistic and morphological engineering of individual perovskite NC emitters (impacting the phonon spectrum, optical coherence, and exciton fine-structure) and exploitation of the vast engineerability of SLs at the mesoscale (diverse SL structures) and at microscale (SL dimensions, positioning, and device-integration) will foster important studies on many-body light-matter interactions in complex lattices such as the Dicke quantum phase transitions<sup>47,48</sup>. Such investigations may yield brighter perovskite NC assemblies or, more intriguingly, may boost the development of massively-entangled multi-photon quantum light sources<sup>49</sup>, which could find applications in optical quantum computing or quantum imaging applications<sup>50,51</sup>.

## References:

1. Spano, F. C. The spectral signatures of Frenkel polarons in H- and J-aggregates. *Acc. Chem. Res.* **43**, 429-439 (2010).
2. Haedler, A. T. *et al.* Long-range energy transport in single supramolecular nanofibres at room temperature. *Nature* **523**, 196-199 (2015).
3. Brédas, J.-L., Sargent, E. H. & Scholes, G. D. Photovoltaic concepts inspired by coherence effects in photosynthetic systems. *Nat. Mater.* **16**, 35-44 (2017).
4. Scheibe, G. Über den Mechanismus der Sensibilisierung photochemischer Reaktionen durch Farbstoffe, insbesondere der Assimilation. *Naturwissenschaften* **25**, 795-795 (1937).
5. Franck, J. & Teller, E. Migration and photochemical action of excitation energy in crystals. *J. Chem. Phys.* **6**, 861-872 (1938).
6. Boles, M. A., Engel, M. & Talapin, D. V. Self-assembly of colloidal nanocrystals: from intricate structures to functional materials. *Chem. Rev.* **116**, 11220-11289 (2016).
7. Protesescu, L. *et al.* Nanocrystals of cesium lead halide perovskites (CsPbX<sub>3</sub>, X=Cl, Br, and I): novel optoelectronic materials showing bright emission with wide color gamut. *Nano Lett.* **15**, 3692-3696 (2015).
8. Kovalenko, M. V., Protesescu, L. & Bodnarchuk, M. I. Properties and potential optoelectronic applications of lead halide perovskite nanocrystals. *Science* **358**, 745-750 (2017).
9. Akkerman, Q. A., Rainò, G., Kovalenko, M. V. & Manna, L. Genesis, challenges and opportunities for colloidal lead halide perovskite nanocrystals. *Nat. Mater.* **17**, 394-405 (2018).
10. Becker, M. A. *et al.* Bright triplet excitons in caesium lead halide perovskites. *Nature* **553**, 189-193 (2018).
11. Becker, M. A. *et al.* Long exciton dephasing time and coherent phonon coupling in CsPbBr<sub>2</sub>Cl perovskite nanocrystals. *Nano Lett.* **18**, 7546-7551 (2018).
12. Utzat, H. *et al.* Coherent single-photon emission from colloidal lead halide perovskite quantum dots. *Science* **363**, 1068-1072 (2019).
13. Rainò, G. *et al.* Superfluorescence from lead halide perovskite quantum dot superlattices. *Nature* **563**, 671-675 (2018).
14. Skribanowitz, N., Herman, I. P., MacGillivray, J. C. & Feld, M. S. Observation of Dicke superradiance in optically pumped HF gas. *Phys. Rev. Lett.* **30**, 309-312 (1973).
15. Miyajima, K., Kagotani, Y., Saito, S., Ashida, M. & Itoh, T. Superfluorescent pulsed emission from biexcitons in an ensemble of semiconductor quantum dots. *J. Phys. Condens. Matter* **21**, 195802 (2009).
16. Malcuit, M. S., Maki, J. J., Simkin, D. J. & Boyd, R. W. Transition from superfluorescence to amplified spontaneous emission. *Phys. Rev. Lett.* **59**, 1189-1192 (1987).
17. Timothy Noe II, G. *et al.* Giant superfluorescent bursts from a semiconductor magneto-plasma. *Nat. Phys.* **8**, 219-224 (2012).
18. Shevchenko, E. V., Talapin, D. V., Kotov, N. A., O'Brien, S. & Murray, C. B. Structural diversity in binary nanoparticle superlattices. *Nature* **439**, 55-59 (2006).
19. Tan, R., Zhu, H., Cao, C. & Chen, O. Multi-component superstructures self-assembled from nanocrystal building blocks. *Nanoscale* **8**, 9944-9961 (2016).
20. Nykypanchuk, D., Maye, M. M., van der Lelie, D. & Gang, O. DNA-guided crystallization of colloidal nanoparticles. *Nature* **451**, 549-552 (2008).
21. Laramy, C. R., O'Brien, M. N. & Mirkin, C. A. Crystal engineering with DNA. *Nat. Rev. Mater.* **4**, 201-224 (2019).
22. Murray, C. B., Kagan, C. R. & Bawendi, M. G. Self-organization of CdSe nanocrystallites into three-dimensional quantum dot superlattices. *Science* **270**, 1335-1338 (1995).

23. Kang, Y., Ye, X. & Murray, C. B. Size- and shape-selective synthesis of metal nanocrystals and nanowires using CO as a reducing agent. *Angew. Chem. Int. Ed.* **49**, 6156-6159 (2010).
24. Kovalenko, M. V. & Bodnarchuk, M. I. Lead halide perovskite nanocrystals: from discovery to self-assembly and applications. *Chimia* **71**, 461-470 (2017).
25. Nagaoka, Y. *et al.* Nanocube superlattices of cesium lead bromide perovskites and pressure-induced phase transformations at atomic and mesoscale levels. *Adv. Mater.* **29**, 1606666 (2017).
26. van der Burgt, J. S. *et al.* Cuboidal supraparticles self-assembled from cubic CsPbBr<sub>3</sub> perovskite nanocrystals. *J. Phys. Chem. C* **122**, 15706-15712 (2018).
27. Baranov, D., Toso, S., Imran, M. & Manna, L. Investigation into the photoluminescence red shift in cesium lead bromide nanocrystal superlattices. *J. Phys. Chem. Lett.* **10**, 655-660 (2019).
28. Chen, Z. & O'Brien, S. Structure direction of II-VI semiconductor quantum dot binary nanoparticle superlattices by tuning radius ratio. *ACS Nano* **2**, 1219-1229 (2008).
29. Coropceanu, I., Boles, M. A. & Talapin, D. V. Systematic mapping of binary nanocrystal superlattices: the role of topology in phase selection. *J. Am. Chem. Soc.* **141**, 5728-5740 (2019).
30. Bodnarchuk, M. I. *et al.* Rationalizing and controlling the surface structure and electronic passivation of cesium lead halide nanocrystals. *ACS Energy Lett.* **4**, 63-74 (2019).
31. Jishkariani, D. *et al.* Nanocrystal core size and shape substitutional doping and underlying crystalline order in nanocrystal superlattices. *ACS Nano* **13**, 5712-5719 (2019).
32. Dong, Y. *et al.* Precise control of quantum confinement in cesium lead halide perovskite quantum dots via thermodynamic equilibrium. *Nano Lett.* **18**, 3716-3722 (2018).
33. Landman, U. & Luedtke, W. D. Small is different: energetic, structural, thermal, and mechanical properties of passivated nanocluster assemblies. *Faraday Discuss.* **125**, 1-22 (2004).
34. Travasset, A. Topological structure prediction in binary nanoparticle superlattices. *Soft Matter* **13**, 147-157 (2016).
35. Travasset, A. Soft skyrmions, spontaneous valence and selection rules in nanoparticle superlattices. *ACS Nano* **11**, 5375-5382 (2017).
36. Evers, W. H. *et al.* Entropy-driven formation of binary semiconductor-nanocrystal superlattices. *Nano Lett.* **10**, 4235-4241 (2010).
37. Boles, M. A. & Talapin, D. V. Many-body effects in nanocrystal superlattices: departure from sphere packing explains stability of binary phases. *J. Am. Chem. Soc.* **137**, 4494-4502 (2015).
38. Dang, N. V., Dang, N. T., Ho, T. A., Tran, N. & Phan, T. L. Electronic structure and magnetic properties of BaTi<sub>1-x</sub>Mn<sub>x</sub>O<sub>3</sub>. *Curr. Appl. Phys.* **18**, 150-154 (2018).
39. Shi, C.-Y., Hao, Y.-M. & Hu, Z.-B. Structural and magnetic properties of single perovskite Ca(Ti<sub>1/2</sub>Mn<sub>1/2</sub>)O<sub>3</sub>. *J. Magn. Magn. Mater.* **323**, 1973-1976 (2011).
40. Vieten, J. *et al.* Materials design of perovskite solid solutions for thermochemical applications. *Energy Environ. Sci.* **12**, 1369-1384 (2019).
41. Evers, W. H., Friedrich, H., Fillion, L., Dijkstra, M. & Vanmaekelbergh, D. Observation of a ternary nanocrystal superlattice and its structural characterization by electron tomography. *Angew. Chem. Int. Ed.* **48**, 9655-9657 (2009).
42. Dong, A., Ye, X., Chen, J. & Murray, C. B. Two-dimensional binary and ternary nanocrystal superlattices: the case of monolayers and bilayers. *Nano Lett.* **11**, 1804-1809 (2011).
43. Paik, T., Diroll, B. T., Kagan, C. R. & Murray, C. B. Binary and ternary superlattices self-assembled from colloidal nanodisks and nanorods. *J. Am. Chem. Soc.* **137**, 6662-6669 (2015).
44. Scheibe, G. Über die Veränderlichkeit der Absorptionsspektren in Lösungen und die Nebenvalenzen als ihre Ursache. *Angew. Chem.* **50**, 212-219 (1937).
45. Jelley, E. E. Spectral absorption and fluorescence of dyes in the molecular state. *Nature* **138**, 1009-1010 (1936).
46. Bonifacio, R. & Lugiato, L. A. Cooperative radiation processes in two-level systems: superfluorescence. *Phys. Rev. A* **11**, 1507-1521 (1975).

47. Baumann, K., Guerlin, C., Brennecke, F. & Esslinger, T. Dicke quantum phase transition with a superfluid gas in an optical cavity. *Nature* **464**, 1301-1306 (2010).
48. Strack, P. & Sachdev, S. Dicke quantum spin glass of atoms and photons. *Phys. Rev. Lett.* **107**, 277202 (2011).
49. Munoz, C. S. *et al.* Emitters of N-photon bundles. *Nat. Photon.* **8**, 550-555 (2014).
50. Wang, H. *et al.* Boson sampling with 20 Input photons and a 60-mode interferometer in a  $10^{14}$ -dimensional Hilbert space. *Phys. Rev. Lett.* **123**, 250503 (2019).
51. Tenne, R. *et al.* Super-resolution enhancement by quantum image scanning microscopy. *Nat. Photon.* **13**, 116-122 (2018).



**Acknowledgements** This work was primarily supported by the European Union through Horizon 2020 Research and Innovation Programme (ERC CoG Grant, grant agreement No. 819740, project SCALE-HALO) and, in part, by the Swiss National Science Foundation (grant No. 200021\_192308, project "Q-Light"). The authors also acknowledge the funding received from EU-H2020 under grant agreement No. 654360 supporting the Transnational Access Activity within the framework NFFA-Europe to the TUG's ELETTRA SAXS beamline of CERIC-ERIC. We thank Y. Shynkarenko for assistance with high-resolution SEM imaging, respectively.

**Author contributions** M.V.K., M.I.B. and G.R. conceived and supervised the project. I.C. performed the synthesis and self-assembly experiments. I.C. and R.E. characterized the materials by electron microscopy. M.B., D.N. and H.A. characterized the materials by GISAXS. G.R., R.F.M. and T.S. carried out optical measurements. A.T. contributed to packing density analysis. I.C. and M.V.K. wrote the manuscript, with input from all authors.

**Competing interests** The authors declare no financial or non-financial competing interests.

#### **Additional information**

**Supplementary Information** is available for this paper.

**Materials & Correspondence** Maksym V. Kovalenko ([mvkovalenko@ethz.ch](mailto:mvkovalenko@ethz.ch))

**Correspondence and requests for materials** should be addressed to M.V.K.

**Reprints and permissions information** is available at <http://www.nature.com/reprints>

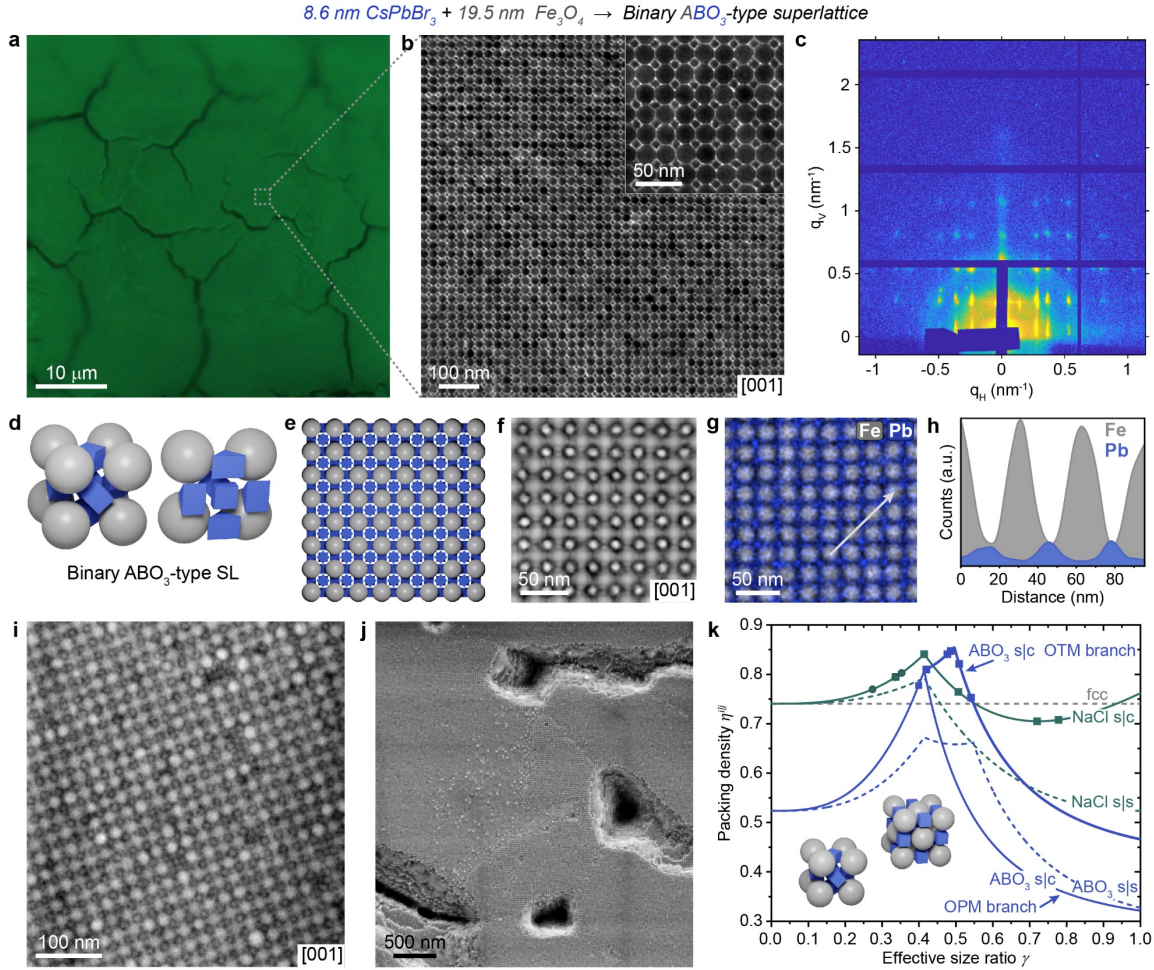


**Fig. 1 | Characterization of a binary ABO<sub>3</sub>-type SL assembled from 8.6 nm CsPbBr<sub>3</sub> and 19.5 nm Fe<sub>3</sub>O<sub>4</sub> NCs ( $\gamma = 0.420$ ).** **a**, Optical microscope image under ultraviolet light. **b**, TEM images of a single [001]<sub>SL</sub>-oriented SL domain. **c**, 2D GISAXS pattern (on a Si<sub>3</sub>N<sub>4</sub>-membrane), showing long-range in- and out-of-plane order in binary SL domains. **d**, ABO<sub>3</sub> unit cell, with Fe<sub>3</sub>O<sub>4</sub> shown as grey spheres and CsPbBr<sub>3</sub> – blue cubes. **e**, Crystallographic model of a [001]<sub>SL</sub>-oriented ABO<sub>3</sub> lattice. **f**, HAADF-STEM image of a [001]<sub>SL</sub>-oriented domain. **g**, EDX-STEM maps for Fe (grey, K-line) and Pb (blue, L-line) and **(h)** respective EDX line scans taken along the line shown in **g**. **i, j**, High- and low-magnification SEM images of [001]<sub>SL</sub>-oriented SL domains. **k**, Calculated space-filling diagrams for ABO<sub>3</sub>- and NaCl-type binary SLs predicted by packing density analysis (OPM, except for indicated OTM-branch); the solid lines mark binary mixtures of larger spheres and smaller cubes (s|c), the dashed lines mark binary mixtures of different spheres (s|s). Experimentally observed ABO<sub>3</sub>- and NaCl-type lattices of this work are represented as dots at the respective  $\gamma$ -values (circles and rectangles denote SLs containing 5.3 and 8.6 nm CsPbBr<sub>3</sub> NCs, respectively). The SL thickness is several hundred nm.

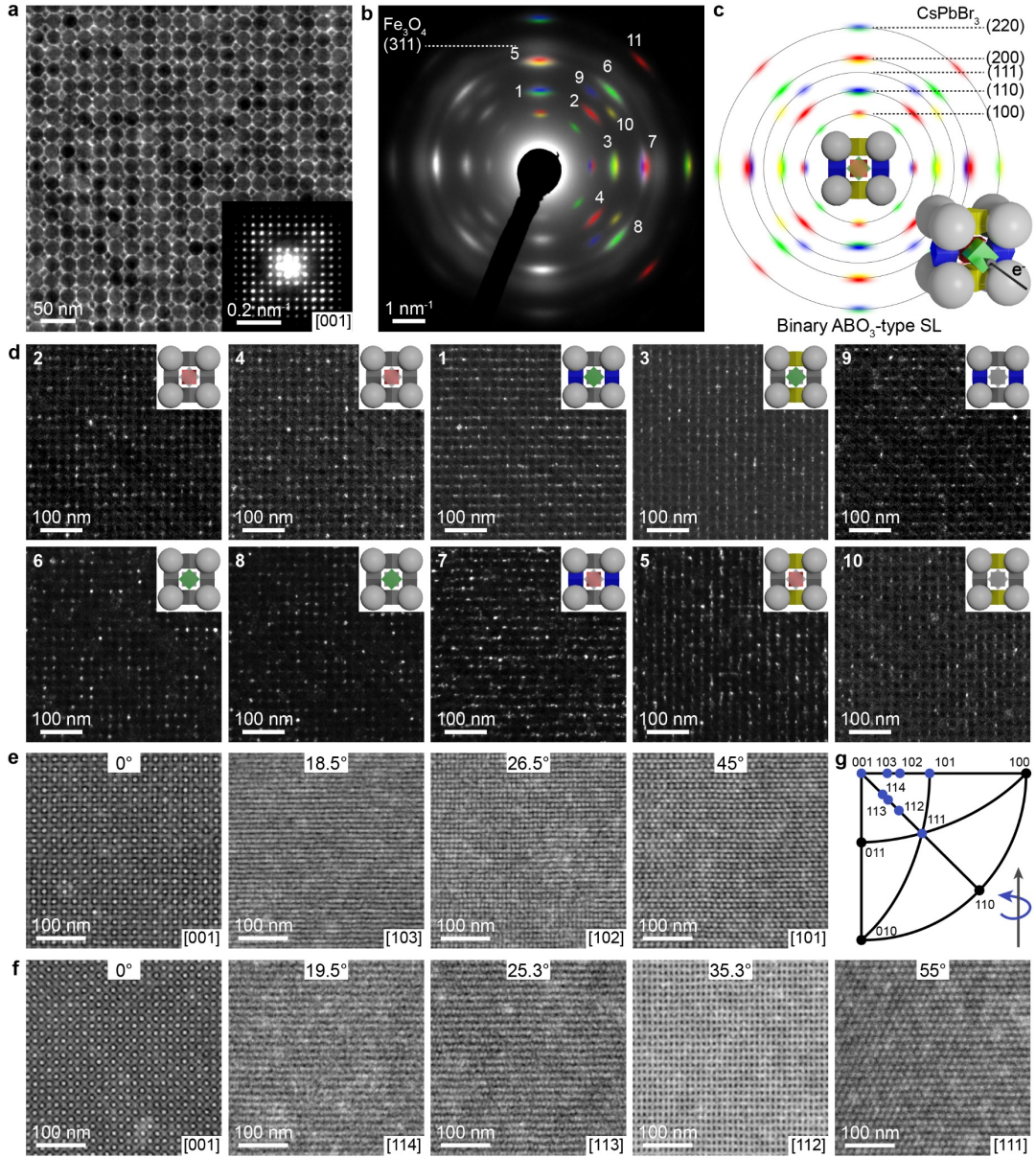


**Fig. 2 | Structural characterization of binary ABO<sub>3</sub>-type SLs.** **a**, TEM image of [001]<sub>SL</sub>-oriented domain assembled from 8.6 nm CsPbBr<sub>3</sub> and 19.5 nm Fe<sub>3</sub>O<sub>4</sub> NCs, along with the corresponding small-angle ED (inset) and **(b)** ED patterns. Owing to the small wavelength of electrons in TEM only lattice planes which are nearly parallel to the incident electron beam contribute to the diffraction pattern. Labelled diffraction arcs in **b** correspond to coloured CsPbBr<sub>3</sub> nanocubes in **c**. **c**, Modeled ED pattern of [001]<sub>SL</sub>-oriented ABO<sub>3</sub>-type binary SL (Fe<sub>3</sub>O<sub>4</sub> reflections are omitted for clarity). The colour of the reflections match the CsPbBr<sub>3</sub> cubes they originate from. The red cube is located in the centre of the lattice and is rotated 45° with respect to the six other cubes, which reside on faces having two CsPbBr<sub>3</sub> <110> directions parallel to <100><sub>SL</sub>. **d**, Dark-field TEM images for the individual kinds of ED reflections numbered in **b**. Coloured cubes in the insets are those observed in the image. **e**, **f**, HAADF-STEM tilting series of the same binary SL domain comprising 14.5 nm Fe<sub>3</sub>O<sub>4</sub> NCs, obtained upon rotation around the [010] and [110] axes, respectively. **g**, Stereograph showing in blue the crystallographic projections of the ABO<sub>3</sub> lattice accessed by tilting.



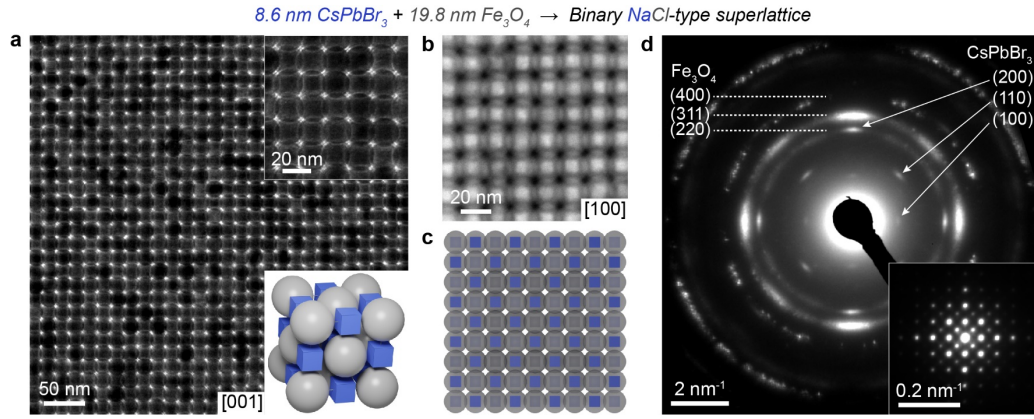


**Fig. 3 | Characterization of NaCl-type binary SL formed from 8.6 nm CsPbBr<sub>3</sub> and 19.8 nm Fe<sub>3</sub>O<sub>4</sub> NCs ( $\gamma = 0.414$ ).** **a**, TEM image of [001]<sub>SL</sub>-oriented NaCl-type SL domain. Top inset is higher magnification image, bottom inset shows NaCl unit cell with the preferable orientation of perovskite cubes. **b**, HAADF-STEM image of [001]<sub>SL</sub>-oriented domain. **c**, Crystallographic model of [001]<sub>SL</sub>-oriented NaCl lattice (opacity of spheres is reduced for clarity). **d**, ED and (inset) small-angle ED pattern of a single domain shown in **a**.

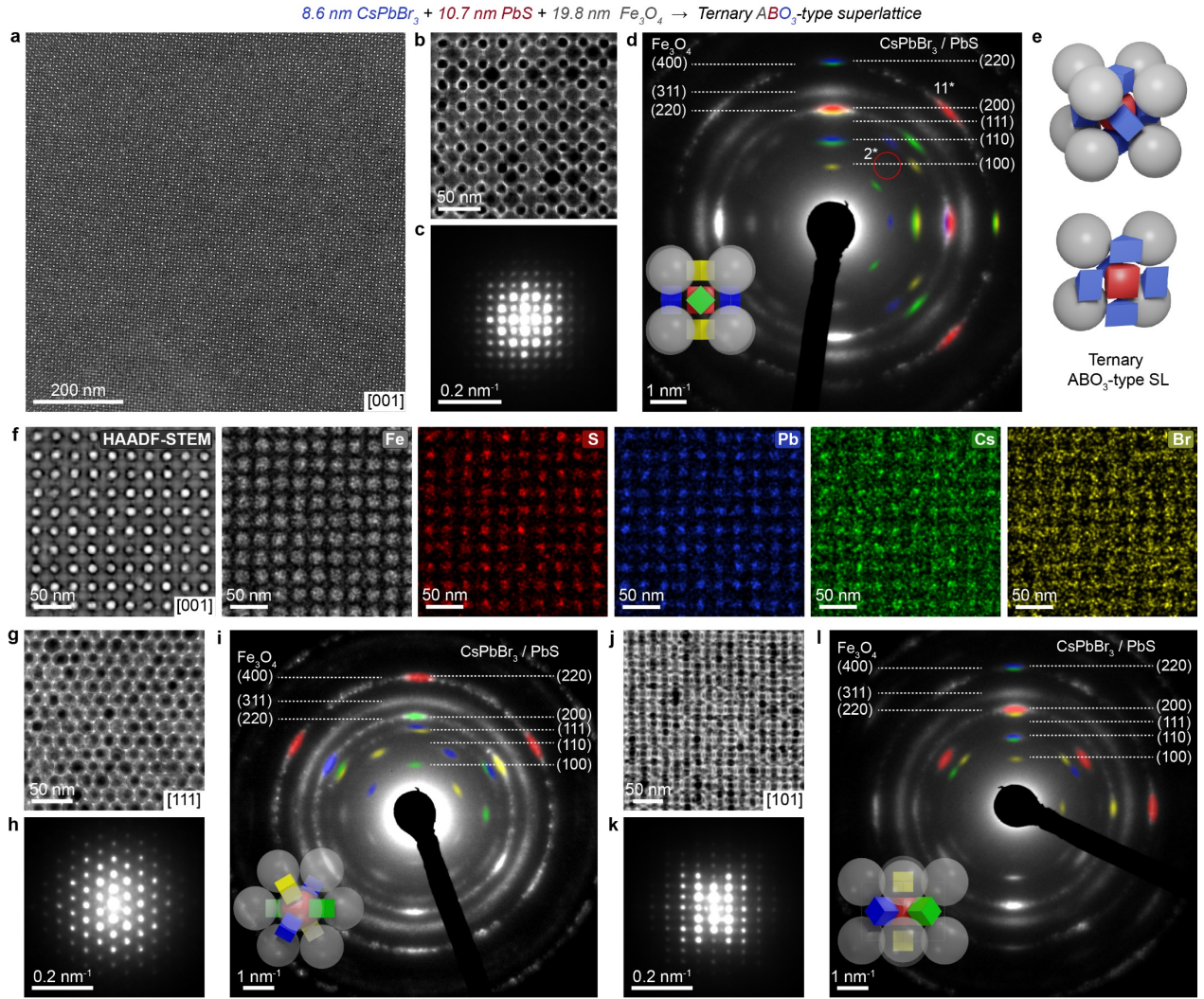


**Fig. 4 | Characterization of ternary ABO<sub>3</sub>-type SL assembled from 8.6 nm CsPbBr<sub>3</sub>, 10.7 nm PbS and 19.8 nm Fe<sub>3</sub>O<sub>4</sub> NCs.** **a**, Large-area HAADF-STEM and **(b)** TEM images of single [001]<sub>SL</sub>-oriented SL domains. **c**, small-angle ED and **(d)** ED patterns measured from the domain shown in **b**. Simultaneous absence of an (110) arc expected from B-site CsPbBr<sub>3</sub> cubes (marked as "2\*", see Fig. 2b for binary SL) and high intensity of the (220) arc ("11\*") point to exclusive occupation of the B-site by PbS NCs. **e**, ABO<sub>3</sub> unit cell, with PbS shown as red bevelled cubes. **f**, HAADF-STEM image and corresponding EDX-STEM maps for Fe (grey, K-line), S (red, K-line), Pb (blue, L-line), Cs (green, L-line) and Br (yellow, K-line). **g**, **j**, TEM images, along with the corresponding **(h, k)** small-angle ED and **(i, l)** ED patterns of single domains in [111]<sub>SL</sub> and [101]<sub>SL</sub> projections, respectively. The origin of CsPbBr<sub>3</sub> and PbS ED reflections in **d, i** and **l** is colour-coded to match the models shown as insets. The appearance of (200) or (220) reflection accompanying the absence of (100) or (110) reflections in the relative directions indicates their origin from PbS NCs and the absence of identically oriented CsPbBr<sub>3</sub> NCs.

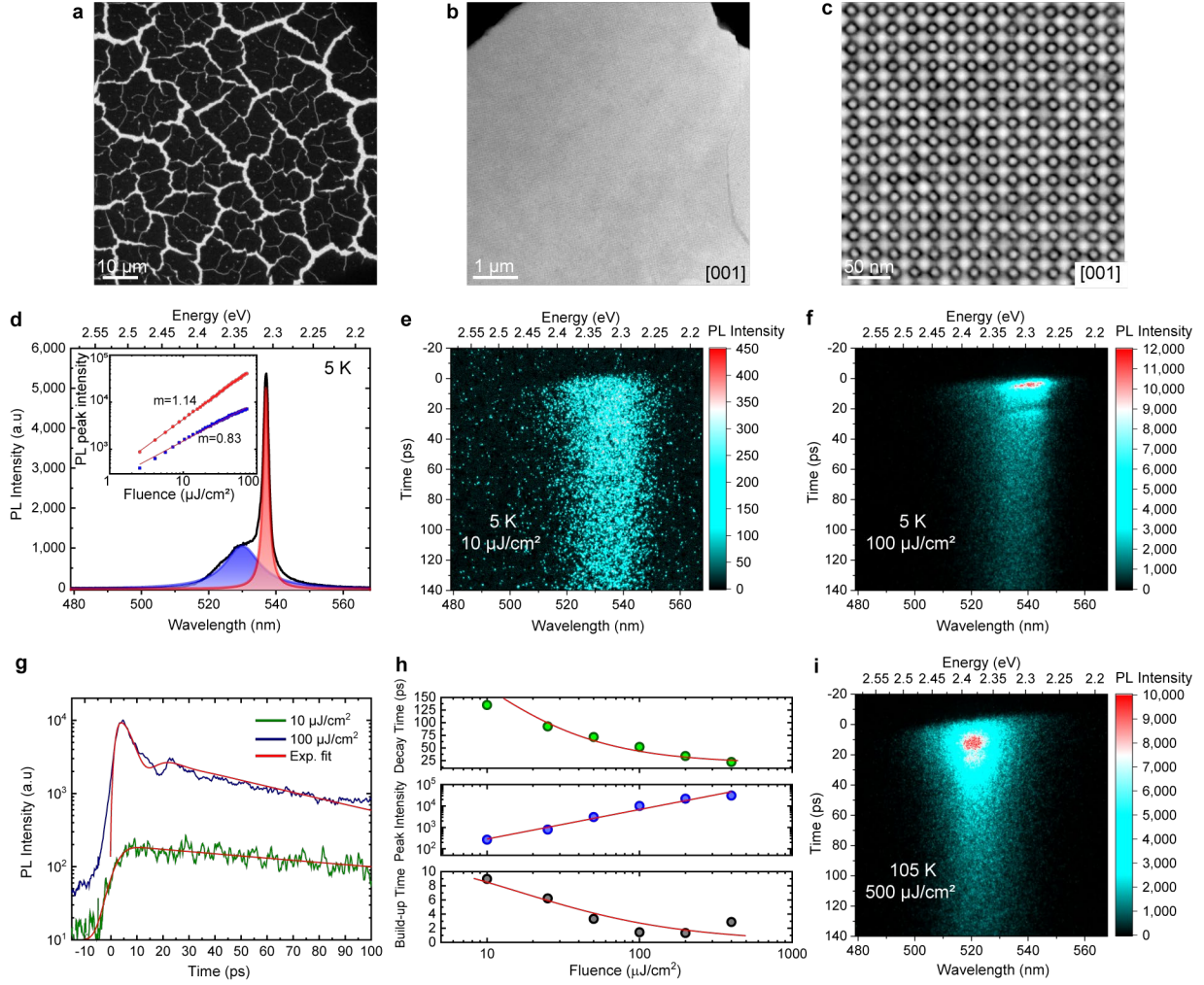


**Fig. 5 | Superfluorescence from ABO<sub>3</sub>-type binary SLs from 8.6 nm CsPbBr<sub>3</sub> and 16.5 nm NaGdF<sub>4</sub>.** **a**, TEM and **(b, c)** HAADF-STEM images. **d**, Emission spectrum, comprising a higher-energy (uncoupled NCs) and a lower-energy band (coupled NCs). The shaded areas are fits to the data using Lorentzian functions, along with (as inset) corresponding integrated PL intensity (red and blue circles) plotted *versus* excitation fluence, where solid lines represent power-law fits with exponents  $m$  of *ca.* 1. **e, f**, Streak camera images obtained with excitation fluences of 10  $\mu\text{J}/\text{cm}^2$  and 100  $\mu\text{J}/\text{cm}^2$ , respectively. **g**, Spectrally-integrated time-resolved emission intensity traces for the two excitation fluences presented in **e** and **f**. Red lines are weighted best-fits to a model that employs an exponential decay function and damped oscillations. **h**, Top, Decay time as a function of the excitation fluence ( $F_{ex}$ ), fitted according to the SF model (red line):  $\tau(F_{ex}) = \frac{\tau_{uncoupled\ NC}}{\zeta F_{ex} + 1} + y_0$ . Here, a fixed value of  $\tau_{uncoupled\ NC} = 350$  ps was used, as found for uncoupled CsPbBr<sub>3</sub> NCs as well as for single NCs. Middle, PL peak intensity at a zero delay time, that increases superlinearly with excitation power, best fitted by a power-law with exponent 1.3 (red line). Bottom, the build-up time (in ps) decreases at high excitation fluences due to the increased interaction among the emitters. The red line is the best fit according the model described in the main text. **i**, Streak camera image obtained with excitation fluence of 500  $\mu\text{J}/\text{cm}^2$  at 105 K.

## Methods.

**Synthesis of CsPbBr<sub>3</sub> NCs.** 8.6 nm were synthesized using oleylamine/oleic acid (OLA/OA) ligand system and then DDAB-treated as described in Ref.<sup>30</sup>. The OLA/OA-synthesis of 5.3 nm CsPbBr<sub>3</sub> NCs was adopted from Ref.<sup>32</sup>. The purified solution of 5.3 nm CsPbBr<sub>3</sub> NCs in toluene/hexane (2 ml, 50%:50% ratio, containing 9 mg NCs) was stirred with DDAB (0.1 ml 0.01 M in toluene) for two hours and used without further purification.

**Synthesis of Fe<sub>3</sub>O<sub>4</sub> NCs.** Oleate-capped iron oxide NCs were synthesized by thermal decomposition of iron oleate complex in octadecene (ODE) according to Ref.<sup>52</sup>. The size of NCs was tuned from 9.6 to 25.1 nm by the OA concentration (from 0.12 to 0.95 M) and reaction temperature (from 308 to 319 °C). After three rounds of purification with hexane and acetone as a solvent/antisolvent pair, the NCs were dispersed in hexane.

**Synthesis of NaGdF<sub>4</sub> NCs.** Hexagonal phase NaGdF<sub>4</sub> NCs were synthesized by thermal decomposition of gadolinium trifluoroacetate in the presence of sodium fluoride in OA/ODE (1 to 1 by volume) mixture at 312 °C for 1 h, adopting reported procedure<sup>53</sup>. Larger NCs were obtained with lower Na-to-Gd ratios. After four washing steps with hexane and ethanol, the NCs were dispersed in hexane.

**Synthesis of truncated cubic PbS NCs.** 10.7 and 11.7 nm PbS NCs were synthesized by the reaction of lead oleate and sulfur at 200 and 205 °C, respectively, following reported procedure<sup>54</sup>. The NCs were washed four times with hexane and ethanol and dispersed in hexane.

**Synthesis of LaF<sub>3</sub> NCs.** 9.2-26.5 nm (diameter) LaF<sub>3</sub> nanodisks were synthesized by thermal decomposition of lanthanum trifluoroacetate in the presence of lithium fluoride in OA/ODE mixture (1:1 by volume) at 300 °C by the varying reaction time, similar to Ref.<sup>43</sup>. After three washing cycles with hexane and ethanol, the NCs were dispersed in hexane.

**Preparation of multicomponent SLs.** Self-assembly of NCs was carried out using a drying-mediated method on three kinds of substrates: carbon-coated TEM grids (carbon type B, Ted Pella, Formvar protective layer was removed by immersing the grid in toluene for 10 s), silicon nitride membranes (TEM windows) and HF-treated silicon. A mixture of NCs in anhydrous toluene had an overall particle concentration of 0.5-2  $\mu$ M and NC number ratios in the range of 0.5-20. 28-35  $\mu$ l of NC mixture was transferred into a tilted 1.5 ml glass vial with a substrate inside. The solvent was evaporated under 0.45 atm pressure at room temperature. For example, binary ABO<sub>3</sub>-, AlB<sub>2</sub>- and NaCl-type SLs with high yields were formed on TEM grids upon slow drying of a solutions prepared by mixing 19.8 nm Fe<sub>3</sub>O<sub>4</sub> NCs (40 mg/ml, 3.5  $\mu$ l) and 8.6 nm CsPbBr<sub>3</sub> NCs (3.0  $\mu$ M; 4.5  $\mu$ l, 2.4  $\mu$ l and 1.6  $\mu$ l, respectively) with anhydrous toluene (25  $\mu$ l).

**Electron microscopy characterization.** TEM and HAADF-STEM images as well as ED and small-angle ED patterns were collected with the use of JEOL JEM2200FS microscope operating at 200 kV accelerating voltage. Owing to the small wavelength of electrons (2.51 pm at 200 keV) the Bragg angles in ED are also small and, as a consequence, only lattice planes which are nearly parallel to the incident electron beam contribute to the diffraction pattern (electron beam is normal to the plane of the ED pattern). EDX-STEM maps and HAADF-STEM images at different tilt angle were recorded using an FEI Titan Themis microscope operated at 300 kV equipped with a SuperEDX detector, with the aid of a motorized dual-axis tomography holder. Electron tomography was carried out in HAADF-STEM mode at 300 kV using a small beam semi-convergence angle of 2.5 mrad, in order to increase the depth of field. Images were recorded over a tilt angle range from -74° to +74° in intervals of 2°. Reconstruction was done using the SIRT algorithm. The tomogram was recorded on a SL slightly inclined in respect to the electron beam, self-assembled on holey carbon coated TEM grid (Agar Scientific). TEM and electron diffraction images were compared with the ones simulated in Crystal Maker 10.4.5 and Single Crystal 3.1.5 software, purchased from CrystalMaker Software Ltd. SEM images were obtained on a FEI Helios 660 operated at 3 kV using immersion mode.

**GISAXS characterization.** GISAXS measurements were performed at the Austrian SAXS beamline of the electron storage ring ELETTRA using a photon energy of 8 keV<sup>55</sup>. The beamline setup was adjusted to a sample-to-detector distance of 1824 mm to result in an accessible horizontal  $q$ -range of  $-1.2 < q_H < 1.8 \text{ nm}^{-1}$  and vertical  $q$ -range of  $-0.1 < q_V < 2.9 \text{ nm}^{-1}$ . The X-ray beam was collimated to a spot-size at sample of approx.  $200 \times 200 \mu\text{m}$ . All images



were recorded using the Pilatus 1M detector (Dectris, Switzerland) with an exposure time of 10 s per image. Reference patterns to calibrate the  $q$ -scale were collected of silver-behenate ( $d$ -spacings of 5.838 nm). Samples were mounted on a 2-axis goniometer stage with  $0.001^\circ$  angular precision, allowing us to ensure an incidence angle of  $0.04^\circ$  for all measurements (determined by alignment of the specular reflection on the detector). All presented data was corrected for fluctuations of the primary intensity. Data treatment was done using the NIKA2D<sup>56</sup> (geometry correction and calibration) as well as GIXSGUI<sup>57</sup> (lattice indexing) software packages.

**Optical properties of CsPbBr<sub>3</sub> NCs.** Optical absorption spectra were measured with Jasco V770 spectrometer in transmission mode. PL spectra were measured in a 90-degree configuration using Horiba Fluoromax-4P+ equipped with a photomultiplier tube and a monochromatized 150 W Xenon lamp as an excitation source. The PL quantum yield of the samples was measured in Hamamatsu Quantaaurus-QY Plus UV-NIR absolute PL spectrometer (C13534-11) equipped with an integrating sphere. The SLs for PL quantum yield measurements were assembled on the square 5 mm  $\times$  5 mm sapphire substrates.

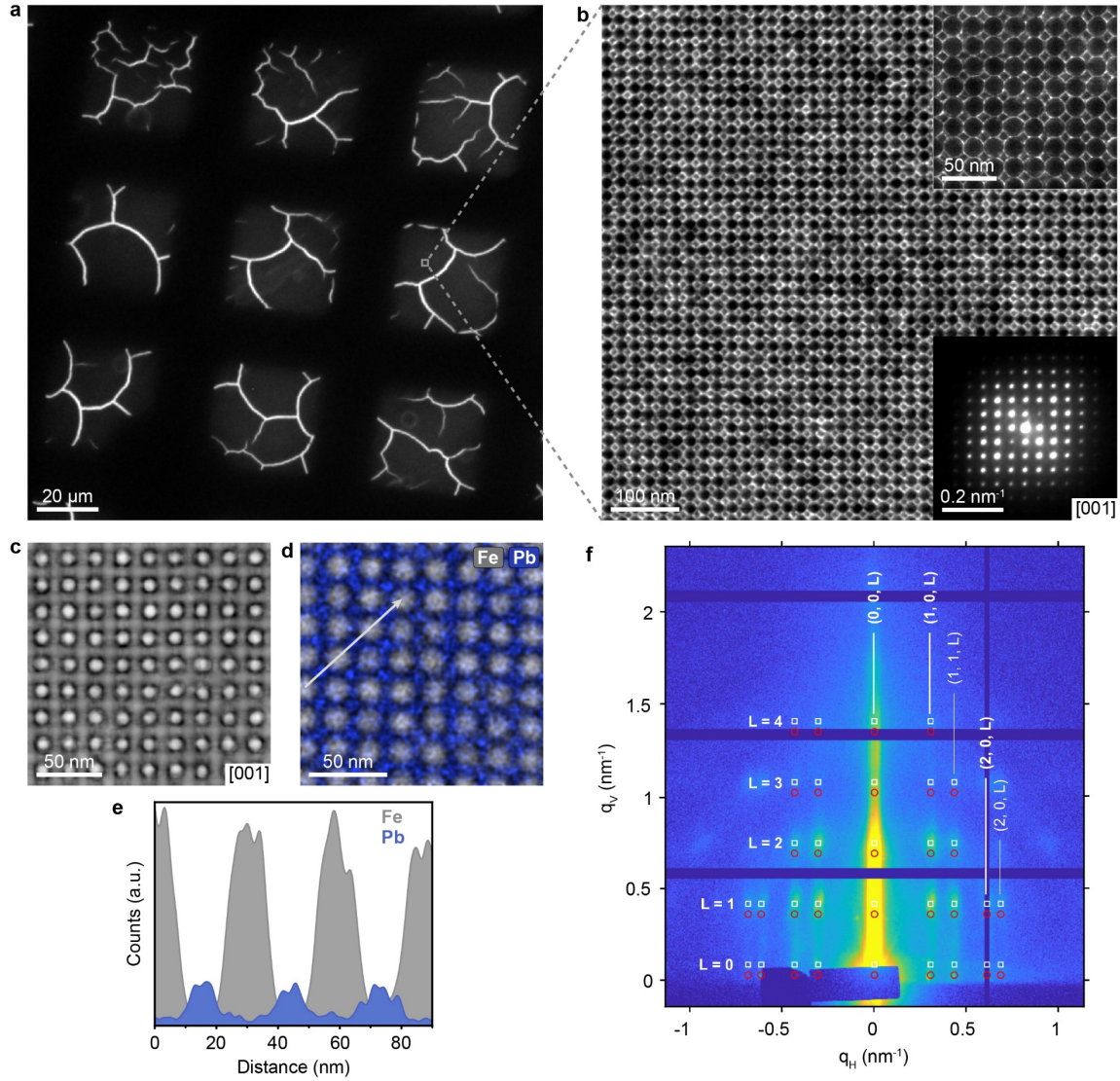
**Optical spectroscopy of SLs.** For PL and time-resolved PL (Fig. 5 and Extended Data Figs. 9, 10), the sample was mounted in a Helium exchange-gas cryostat at 5 K (or higher temperature by using a heater when otherwise specified). A frequency-doubled regenerative amplifier seeded with a mode-locked Ti:sapphire laser with a pulse duration of 100–200 fs and a repetition rate of 1 kHz at 3.1 eV photon energy was used as excitation source after passing through short-pass filters (442 nm cut-off wavelength). For both excitation and detection, we used the same focusing lens with 100 mm focal length, resulting in an excitation spot radius of about 60  $\mu$ m. The recorded PL was long-pass filtered (480 nm cut-off wavelength) and then dispersed by a grating with 150 lines per mm in a 0.3 m-long monochromator and detected with a streak camera with nominal time resolution of 2 ps and instrument response function FWHM of 4 ps. The time-integrated PL spectra were recorded by a 0.5 m-long spectrograph with a grating with 300 lines per mm and a nitrogen-cooled CCD camera.

52. Park, J. *et al.* Ultra-large-scale syntheses of monodisperse nanocrystals. *Nat. Mater.* **3**, 891-895 (2004).
53. Paik, T., Ko, D. K., Gordon, T. R., Doan-Nguyen, V. & Murray, C. B. Studies of liquid crystalline self-assembly of GdF<sub>3</sub> nanoplates by in-plane, out-of-plane SAXS. *ACS Nano* **5**, 8322-8330 (2011).
54. Ibanez, M. *et al.* Electron doping in bottom-up engineered thermoelectric nanomaterials through HCl-mediated ligand displacement. *J. Am. Chem. Soc.* **137**, 4046-4049 (2015).
55. Amenitsch, H., Bernstorff, S. & Laggner, P. High-flux beamline for small-angle x-ray scattering at ELETTRA. *Rev. Sci. Instrum.* **66**, 1624-1626 (1995).
56. Ilavsky, J. Nika: software for two-dimensional data reduction. *J. Appl. Cryst.* **45**, 324-328 (2012).
57. Jiang, Z. GIXSGUI: a MATLAB toolbox for grazing-incidence X-ray scattering data visualization and reduction, and indexing of buried three-dimensional periodic nanostructured films. *J. Appl. Cryst.* **48**, 917-926 (2015).

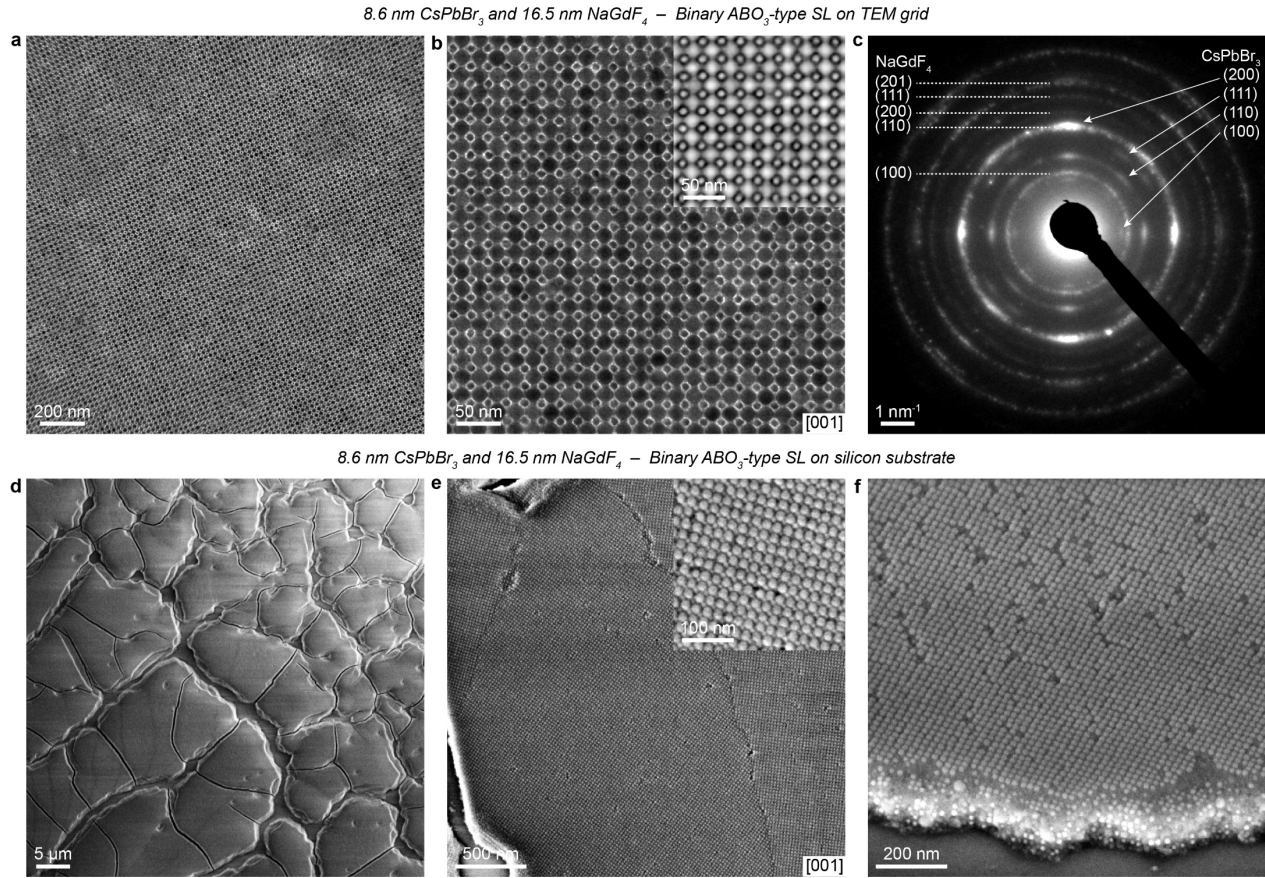
#### Data availability

*The data that support the findings of this study are available from the corresponding author upon reasonable request.*

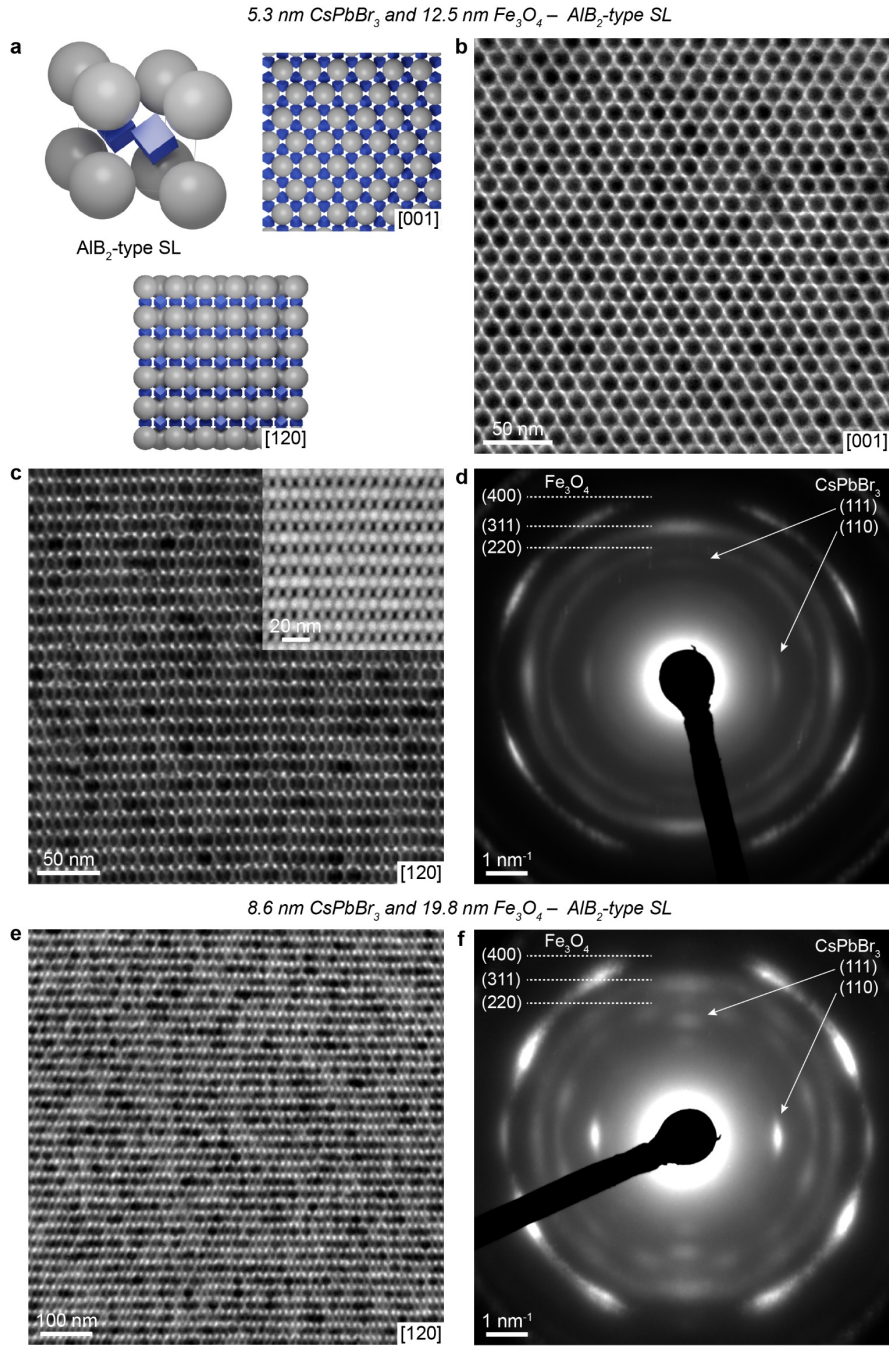




**Extended Data Fig. 1 | Structural characterization of a binary ABO<sub>3</sub>-type SL comprising 8.6 nm CsPbBr<sub>3</sub> and 14.5 nm Fe<sub>3</sub>O<sub>4</sub> NCs ( $\gamma = 0.541$ ).** **a**, Low magnification TEM image showing large size of SL domains and homogeneous coverage over carbon-coated TEM grid. **b**, Zoomed-in TEM image from the area indicated by the box in **a**; upper inset presents higher-magnification TEM image; bottom inset is a small-angle ED pattern from a single SL domain in [001]<sub>SL</sub> projection. **c**, HAADF-STEM image of a [001]<sub>SL</sub>-oriented domain. **d**, EDX elemental maps of a [001]<sub>SL</sub>-oriented domain for Fe (grey, K-line) and Pb (blue, L-line). **e**, EDX line scans taken along the line shown in **d**. **f**, 2D GISAXS pattern showing long-range order. The SL reflections can be indexed using a tetragonal (*P4/mmm*) lattice: white markers correspond to the theoretical diffraction peak positions of an  $a = b = 20.5$  nm and  $c = 19.0$  nm unit cell (red markers show the corresponding Laue-type diffraction pattern).

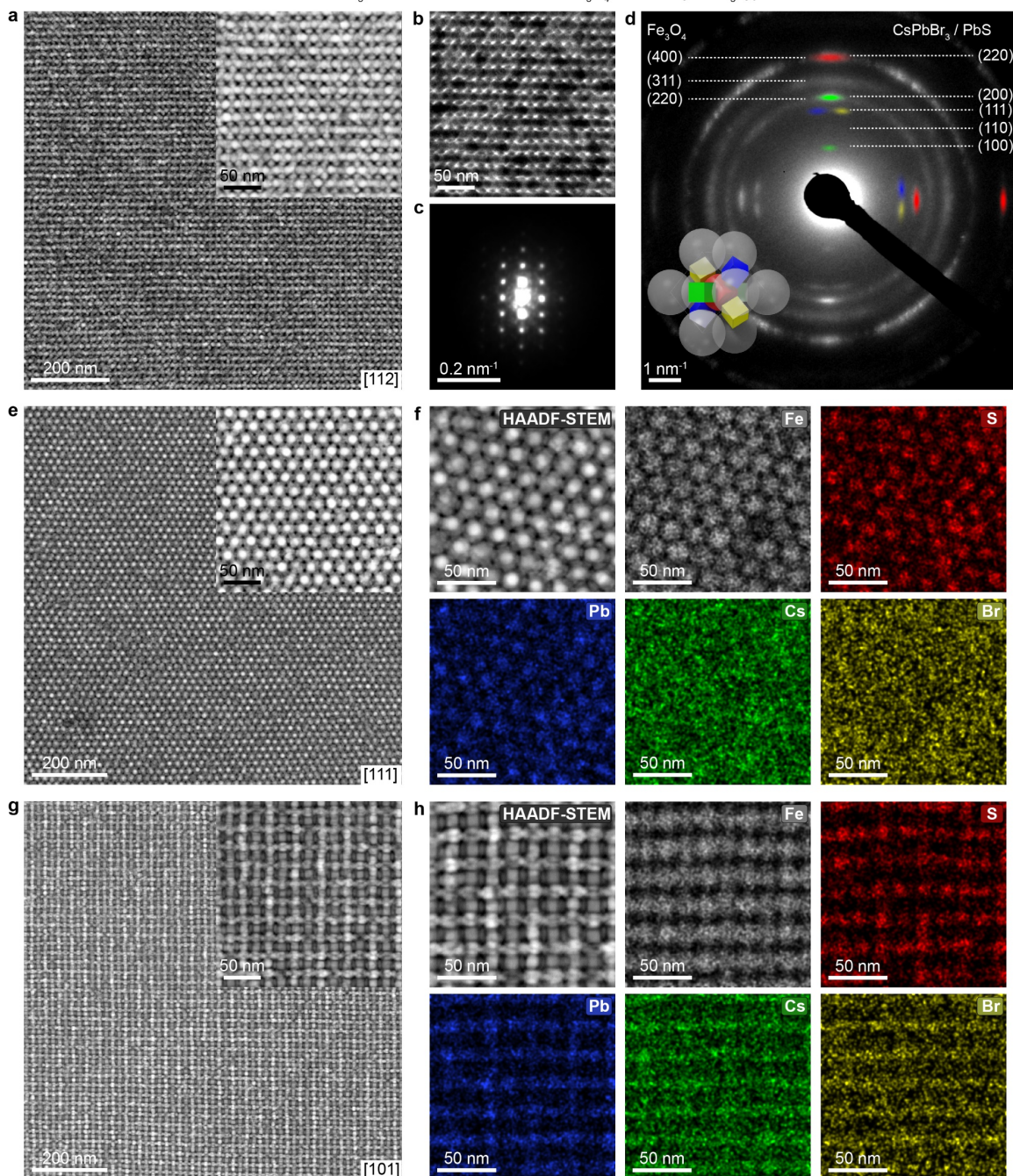


**Extended Data Fig. 2 | Binary ABO<sub>3</sub>-type SL assembled from 8.6 nm CsPbBr<sub>3</sub> and 16.5 nm NaGdF<sub>4</sub> NCs ( $\gamma = 0.486$ ).** **a, b,** TEM images at different magnification of a SL domain deposited on carbon-coated TEM grid, inset in **b** is HAADF-STEM image. **c,** ED pattern from an area displayed in **b**. ED reflections from CsPbBr<sub>3</sub> confirm ABO<sub>3</sub> structure of the SL. **d, e** SEM images at different magnification showing large-area coverage of the silicon substrate by binary SL domains. **f,** Tilted SEM image revealing thickness of the SL domain. PL quantum yield of ABO<sub>3</sub>-type binary SL assembled from 8.6 nm CsPbBr<sub>3</sub> and 16.5 nm NaGdF<sub>4</sub> NCs on sapphire substrates is ~50% and rises above 70% upon cooling with liquid nitrogen.

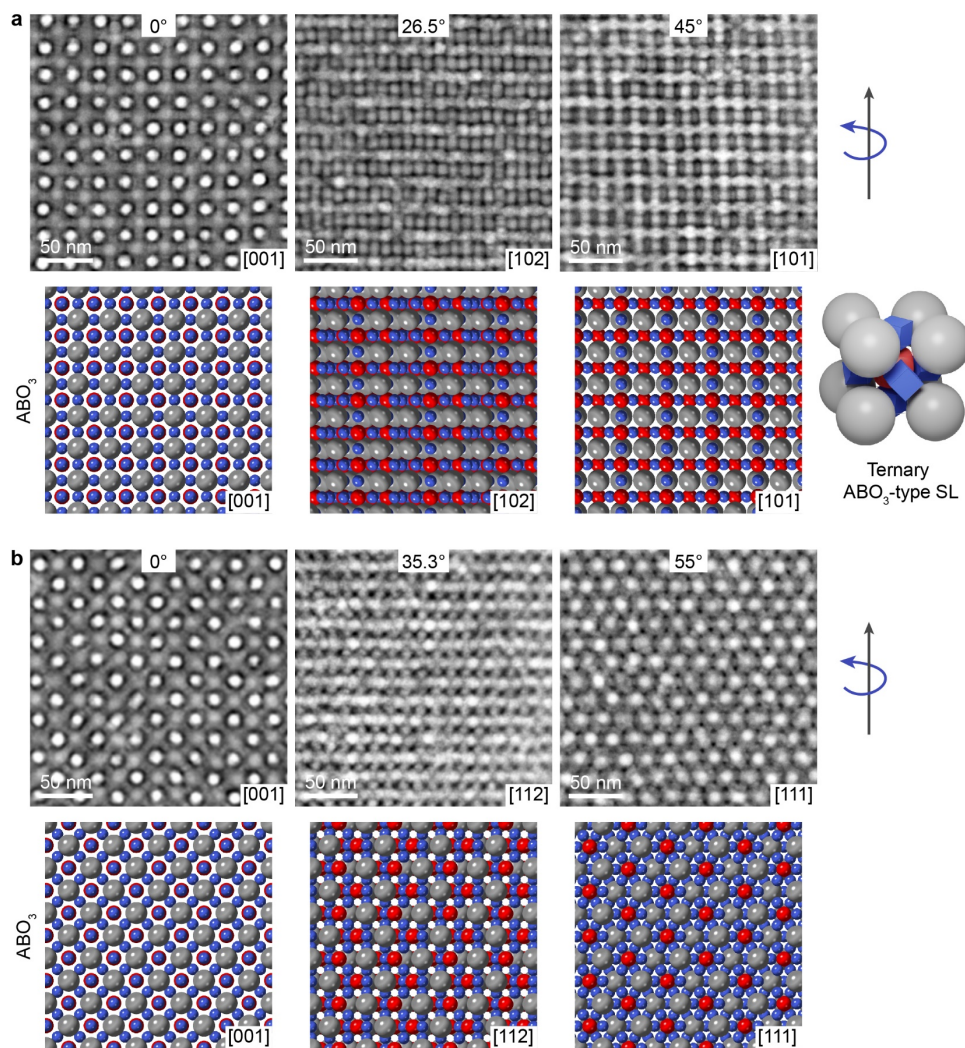


**Extended Data Fig. 3 | AIB<sub>2</sub>-type binary SLs from (b-d) 5.3 nm CsPbBr<sub>3</sub> NCs combined with 12.5 nm Fe<sub>3</sub>O<sub>4</sub> NCs ( $\gamma = 0.353$ ) and (e, f) 8.6 nm CsPbBr<sub>3</sub> NCs combined with 19.8 nm Fe<sub>3</sub>O<sub>4</sub> NCs ( $\gamma = 0.414$ ).** **a**, AIB<sub>2</sub> unit cell, along with crystallographic models of [001]- and [120]-oriented AIB<sub>2</sub> lattices. Fe<sub>3</sub>O<sub>4</sub> shown as grey spheres and CsPbBr<sub>3</sub> – blue cubes. **b**, TEM image of a SL domain in [001]<sub>SL</sub> orientation. **c**, **e**, TEM images of SL domains in [120]<sub>SL</sub> orientation, along with the corresponding (**d**, **f**) ED patterns; inset in **c** shows HAADF-STEM image. The presence of orthogonal reflections from (110) and (111) lattice planes of CsPbBr<sub>3</sub> indicates alignment of nanocubes within the SL such that [111] and [110] crystallographic directions of CsPbBr<sub>3</sub> orient along [001]<sub>SL</sub> and [100]<sub>SL</sub>, respectively.



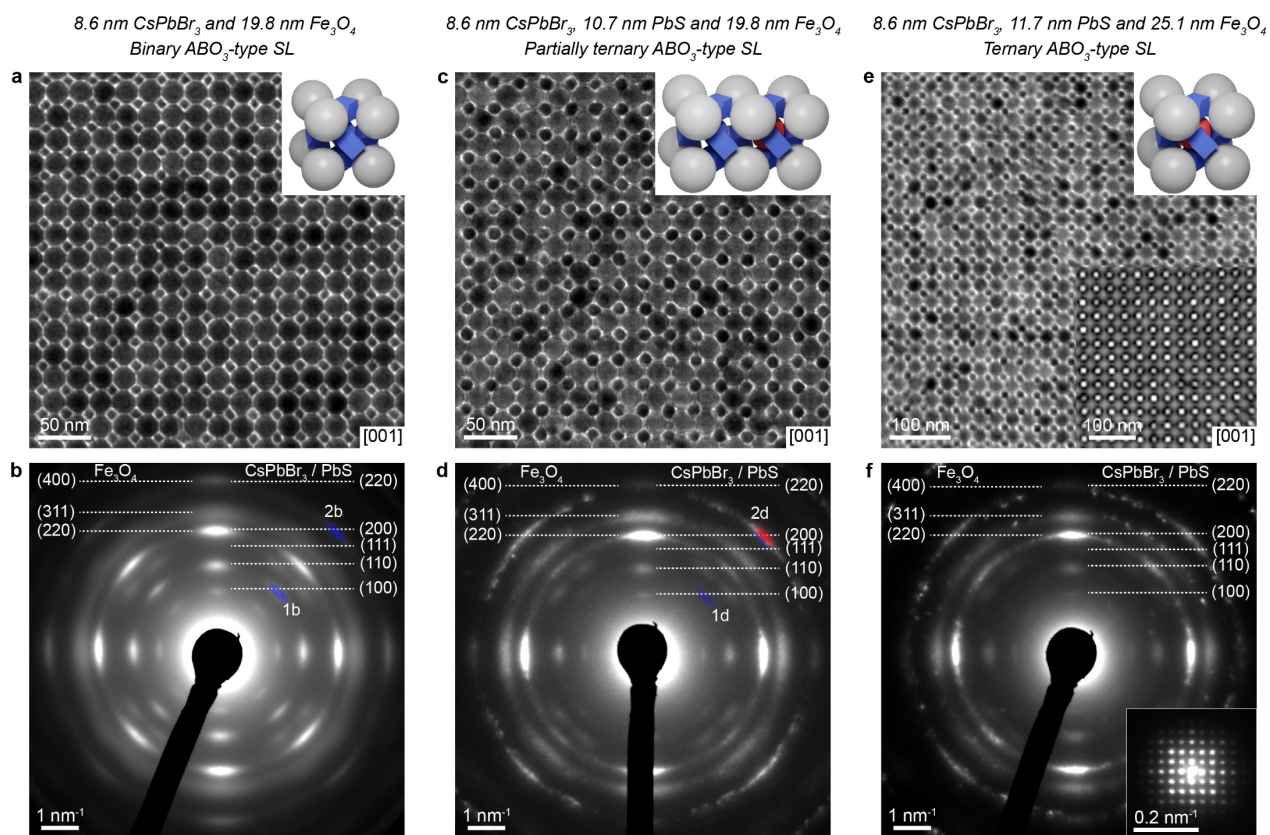


**Extended Data Fig. 4 | Ternary ABO<sub>3</sub>-type SL domains with (a-d) [112]<sub>SL</sub>, (e, f) [111]<sub>SL</sub> and (g, h) [110]<sub>SL</sub> crystallographic orientations assembled from 8.6 nm CsPbBr<sub>3</sub>, 10.7 nm PbS NCs and 19.8 nm Fe<sub>3</sub>O<sub>4</sub> NCs. a, e, g, HAADF-STEM images; insets show higher magnification images. b, TEM image of the [112]<sub>SL</sub>-oriented domain, along with the corresponding (c) small-angle ED and (d) ED patterns; colour of diffraction arcs matches the NC orientations sketched as an inset (electron beam is normal to the plane of view). f, h, HAADF-STEM images and corresponding EDX-STEM maps for Fe (grey, K-line), S (red, K-line), Pb (blue, L-line), Cs (green, L-line) and Br (yellow, K-line).**

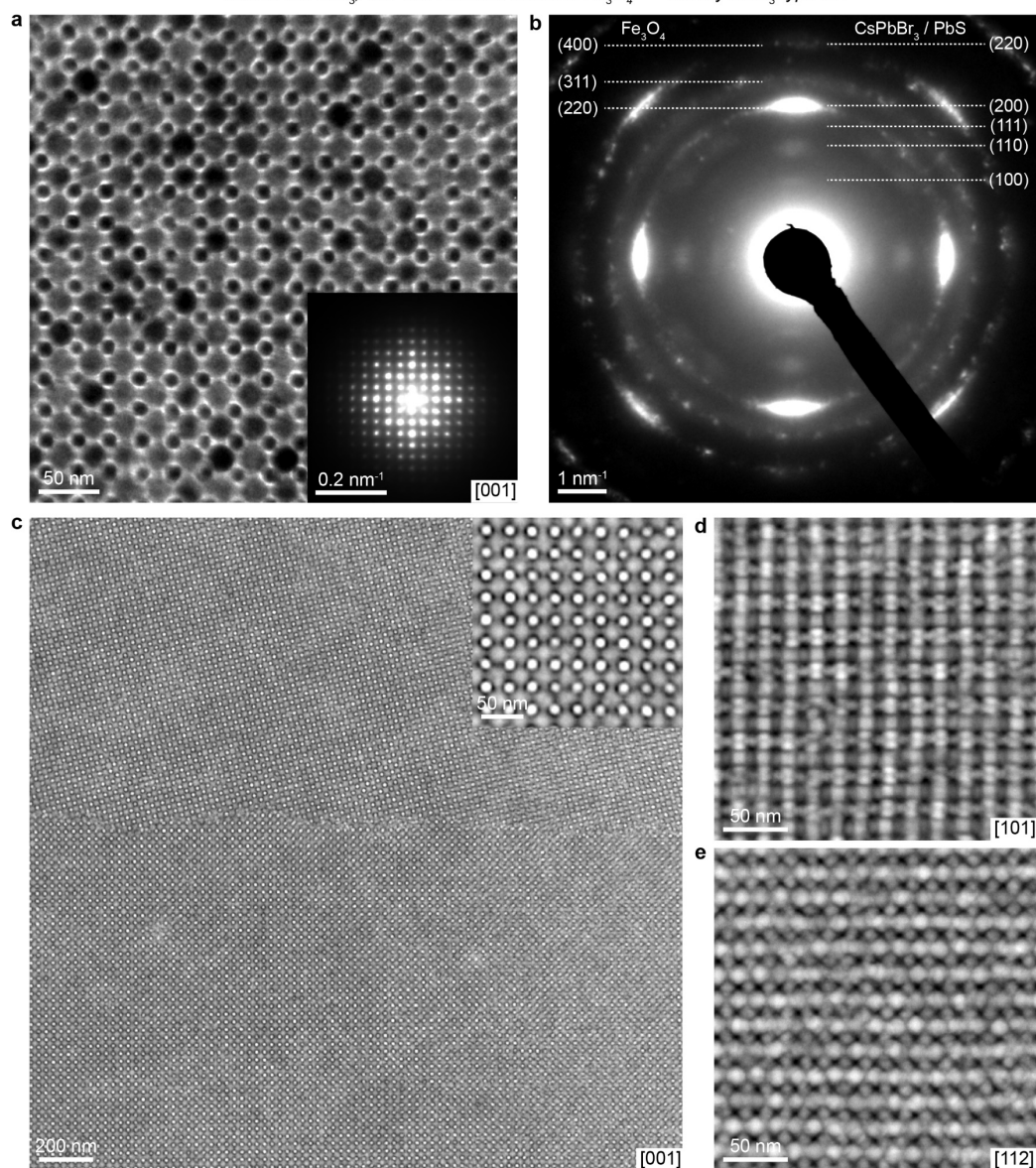


**Extended Data Fig. 5 | HAADF-STEM tilting series around (a)  $[010]_{SL}$  and (b)  $[110]_{SL}$  axes of a ternary  $ABO_3$ -type SL comprising 8.6 nm  $CsPbBr_3$ , 10.7 nm  $PbS$  and 19.8 nm  $Fe_3O_4$  NCs. HAADF-STEM images of a SL domain at different tilting angles match well the corresponding projections of the  $CaTiO_3$  structure.**

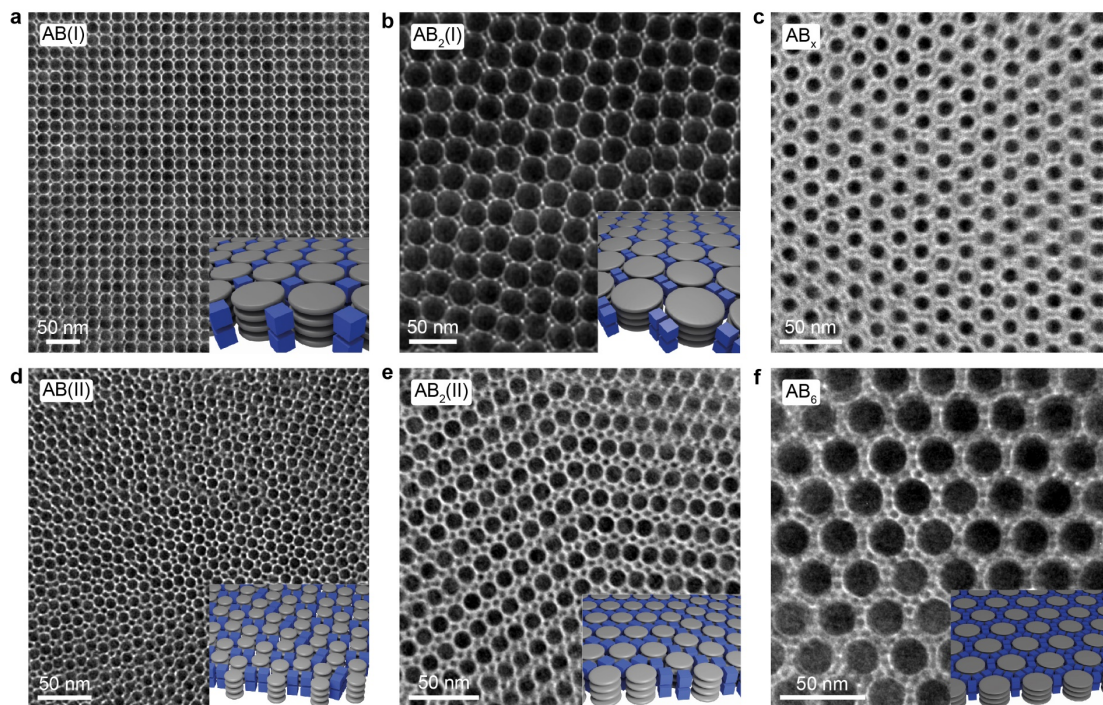




**Extended Data Fig. 6 | Transition from binary ABO<sub>3</sub> SL comprising 8.6 nm CsPbBr<sub>3</sub> NCs and 19.8 nm Fe<sub>3</sub>O<sub>4</sub> NCs to ternary ABO<sub>3</sub> SL comprising 8.6 nm CsPbBr<sub>3</sub> NCs and 25.1 nm Fe<sub>3</sub>O<sub>4</sub> upon incorporation of 10.7-11.7 nm truncated cubic PbS NCs.** **a**, TEM image and corresponding **(b)** ED pattern of a single binary [001]<sub>SL</sub>-oriented domain assembled from 8.6 nm CsPbBr<sub>3</sub> and 19.8 nm Fe<sub>3</sub>O<sub>4</sub> NCs; inset in **a**: model of binary ABO<sub>3</sub> lattice. **c**, TEM image and corresponding **(d)** ED pattern of a single ternary [001]<sub>SL</sub>-oriented domain assembled from 8.6 nm CsPbBr<sub>3</sub> NCs, 10.7 nm PbS NCs and 19.8 nm Fe<sub>3</sub>O<sub>4</sub> NCs; inset in **c**: model of ternary ABO<sub>3</sub> structure showing the formation of solid solution by substitution of CsPbBr<sub>3</sub> NCs on the B-site of the lattice by PbS NCs. The number ratio of PbS to CsPbBr<sub>3</sub> NCs in the mixture is too small to form exclusively ternary SL, as a result, both CsPbBr<sub>3</sub> and PbS NCs are present on B-sites as is evident from ED patterns. In the ED of partially ternary lattice the intensity of (110) reflection "1d", which originates only from centre CsPbBr<sub>3</sub>, is weakened, compared to reflection "1b" in ED of binary SL, since the number of perovskite NCs on B-sites is reduced. Whereas the intensity of (220) reflection "2d" which originates from both CsPbBr<sub>3</sub> and PbS NCs located on B-sites is enhanced compared to reflection "2b" in ED of binary SL, as the scattering from PbS NCs, which contribute to this peak, is stronger than from CsPbBr<sub>3</sub> lattice. As the degree of substitution increases, (111), (200), and (220) ED reflections for CsPbBr<sub>3</sub> and PbS NCs add up (because of similar lattice parameters) and give rise to higher intensity, while the (100) and (110) reflections, to which PbS NCs do not contribute due to their *Fm* $\bar{3}$ *m* symmetry, eventually vanish (see also Fig. 4d and Supplementary Figs. 5q, t). **e**, TEM and HAADF-STEM (bottom inset) images of a single ternary [001]<sub>SL</sub>-oriented ABO<sub>3</sub> domain assembled from 8.6 nm CsPbBr<sub>3</sub>, 11.7 nm PbS and 25.1 nm Fe<sub>3</sub>O<sub>4</sub> NCs, along with the respective **(f)** ED and (inset) small-angle ED patterns; upper inset in **e**: model of ternary ABO<sub>3</sub> lattice. 25.1 nm Fe<sub>3</sub>O<sub>4</sub> NCs are too large to form binary ABO<sub>3</sub>-type SL, however the addition of 11.7 nm truncated cubic PbS NCs makes stable ternary ABO<sub>3</sub>-type SL.

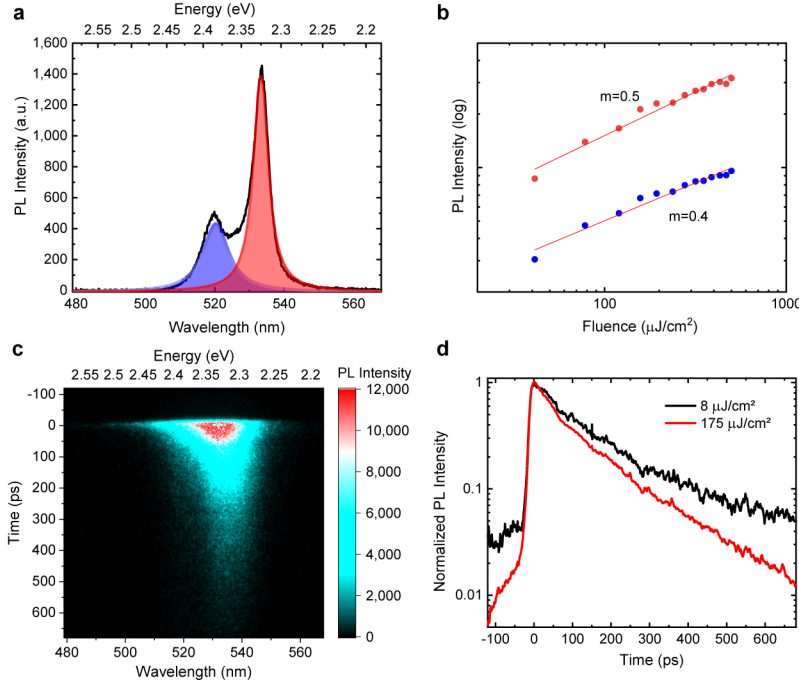


**Extended Data Fig. 7 | Ternary ABO<sub>3</sub>-type SL domains assembled from 8.6 nm CsPbBr<sub>3</sub>, 11.7 nm PbS NCs and 21.5 nm Fe<sub>3</sub>O<sub>4</sub> NCs. a**, TEM image of a single SL domain in [001]<sub>SL</sub> orientation, together with the corresponding (inset) small-angle ED and (b) ED patterns. **c**, Low and high magnification HAADF-STEM images of [001]<sub>SL</sub>-oriented domains. **d**, **e**, HAADF-STEM images of [101]<sub>SL</sub>- and [112]<sub>SL</sub>-oriented domains, respectively.

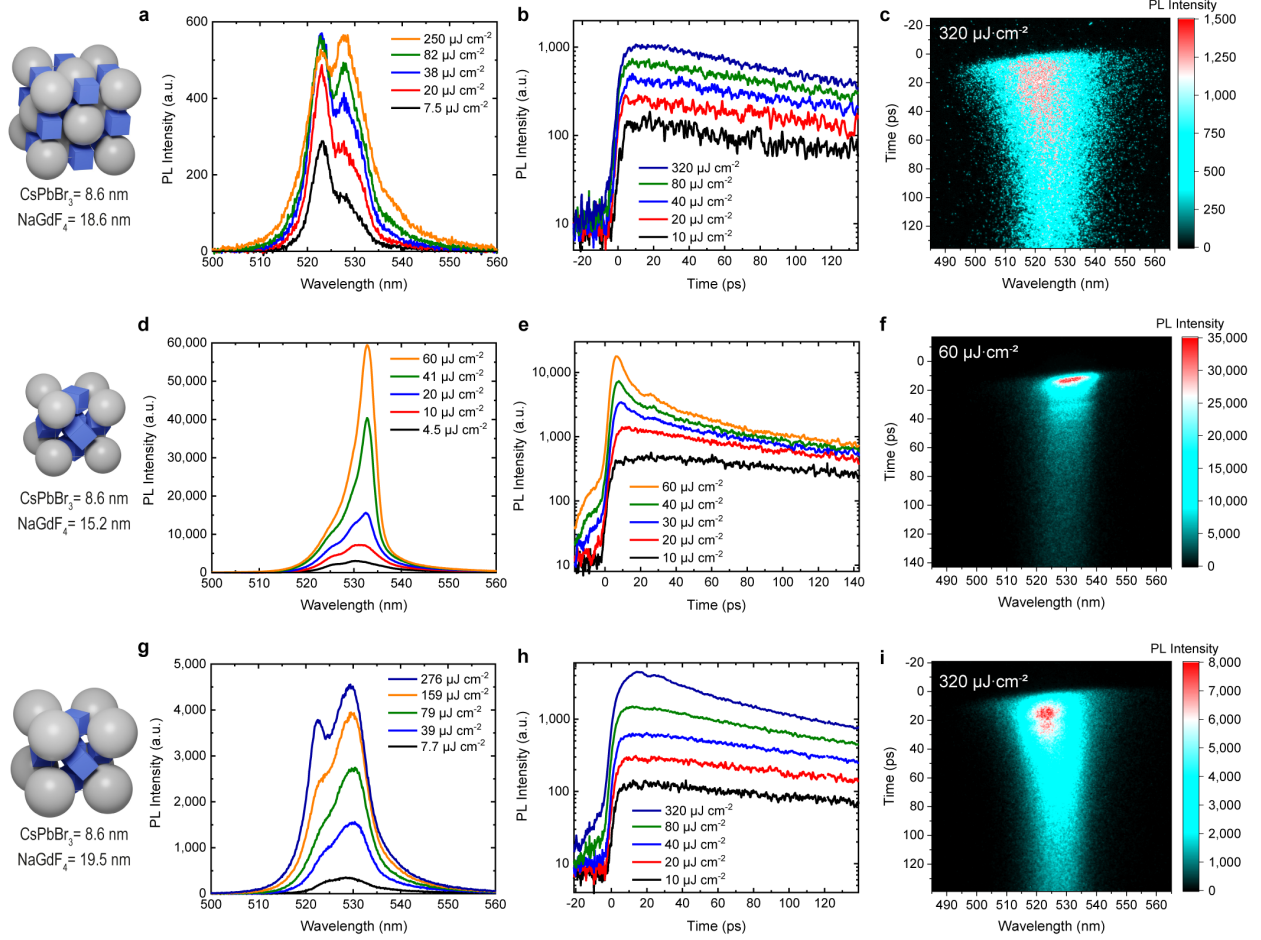


**Extended Data Fig. 8 | TEM images and structural models of columnar binary SLs assembled from 5.3 nm CsPbBr<sub>3</sub> cubes and LaF<sub>3</sub> nanodisks. a, AB(I)-type SL comprising 16.6 nm LaF<sub>3</sub> NCs. b, AB<sub>2</sub>(I)-type SL comprising 26.5 nm LaF<sub>3</sub> NCs. c, AB<sub>x</sub>-type SL comprising 12.5 nm LaF<sub>3</sub> NCs. d, AB(II)-type SL comprising 9.2 nm LaF<sub>3</sub> NCs. e, AB<sub>2</sub>(II)-type SL comprising 12.5 nm LaF<sub>3</sub> NCs. f, AB<sub>6</sub>-type SL comprising 21.0 nm LaF<sub>3</sub> NCs. Six different columnar structures have been observed, as a result of adjusting the cube-to-disk size- and number-ratios. Interestingly, none of these structures had been reported for disks + spheres systems and also not observed by us, highlighting the crucial role that cubic shape plays for the formability of these structures (due to much higher resulting packing density compared to disks + spheres). The yield and the lateral extent of the SL grains are, however, considerably smaller than those of ABO<sub>3</sub>- and NaCl-type SLs and require further optimization.**





**Extended Data Fig. 9 | Luminescence spectroscopy of ABO<sub>3</sub>-type binary SLs, made from 8.6 nm CsPbBr<sub>3</sub> and 16.5 nm NaGdF<sub>4</sub> NCs, on a carbon-coated Cu grid.** **a**, PL spectrum where similarly to Fig. 5 of the Main Text, the PL spectrum is composed of two bands (coupled and uncoupled NCs). **b**, PL intensity for the uncoupled NCs (blue circles) and coupled NCs (red circles) bands, in a log-log plot. Fits to the data (red solid lines) reveal a sub-linear behaviour, with fitted power-law exponents  $m$  of approximately 0.4-0.5, unlike to Si<sub>3</sub>N<sub>4</sub> as a substrate, attesting the occurrence of non-radiative processes at higher fluences, pointing to much enhanced SL-substrate interaction in the case of a conductive carbon film. **c**, Streak camera images obtained with an excitation fluence of 175  $\mu\text{J}/\text{cm}^2$ . Contrary to the results reported in the Main Text for ABO<sub>3</sub>-type SLs on Si<sub>3</sub>N<sub>4</sub>-membranes, no evidence of drastic shortening or time oscillations could be found. Furthermore, a pronounced dynamic redshift characterizes the initial decay which could be related to thermal effects (rapid cooling after heating through the excitation pulse). This is in stark contrast with typical SF spectral dynamic, reported in Fig. 5 of the Main Text and in Ref.<sup>13</sup>, which exhibits a dynamic blueshift *versus* time<sup>13</sup>. **d**, Spectrally-integrated time-resolved emission intensity traces for two excitation fluences, 8  $\mu\text{J}/\text{cm}^2$  and 175  $\mu\text{J}/\text{cm}^2$  respectively. Although a slight shortening of the decay is clearly observed, this is probably due to a non-radiative process, presumably energy transfer to the substrate, given the sublinear fluence-dependence observed in **b** and reduction of fluorescence lifetime of uncoupled NCs from 350 ps to about 100 ps even at low fluences. Carbon-coated grids might introduce absorbing states, which strongly influence the exciton dynamics and the onset of SF emission. This pronounced substrate effect is unsurprising given that SLs are morphologically two-dimensional, being  $\leq 10$  unit cells in thickness.



**Extended Data Fig. 10 | Emission properties of different binary SLs comprising 8.6 nm perovskite NCs.** Fluence-dependent PL and time-resolved PL traces for (a, b) NaCl-type SLs employing 18.6 nm NaGdF<sub>4</sub> NCs, (d, e) ABO<sub>3</sub>-type SLs employing 15.2 nm NaGdF<sub>4</sub> NCs and (g, h) ABO<sub>3</sub>-type SLs employing 19.5 nm NaGdF<sub>4</sub> NCs. Typical streak camera images obtained at high fluences are reported in c, f, i for NaCl- and ABO<sub>3</sub>-type SLs, respectively. See Supplementary Note 4 for the discussion of results.